Polymorphism-Dependent Room-Temperature Phosphorescence of a Persulfurated Benzene

Simone d'Agostino,[a] Andrea Vitale,[a] Yashraj Kapadiya,[b] Marc Gingras,[b]* Fabrizia Negri, [a]* Paola Ceroni[a] and Andrea Fermi[a]**

[a] Dipartimento di Chimica "Giacomo Ciamician", Alma Mater Studiorum−Università di Bologna, via Gobetti 85 – 40129 Bologna, Italy.

[b] Aix Marseille Univ., CNRS, CINAM, Marseille, France

Electronic Supporting Information

Synthesis

General information: **Materials and General Procedures**: All reagents, solvents and chemicals were purchased from Sigma-Aldrich or TCI Europe and used directly unless otherwise stated (purity: reagent or analytical grade). Solvents were stored for several days over freshly activated 3Å or 4Å molecular sieves (activated for 3 hours at 250°C). Reactions were monitored by TLC, ^{1}H, ^{13}C NMR spectroscopy. Thin-Layer chromatography (TLC): TLC analyses were performed on precoated silica gel (Alugram® SilG/UV254gel) aluminium plates from Macherey-Nagel. Compounds were visualized with UV-light (254 or 365 nm). **NMR spectroscopy (CINaM, Aix-Marseille Univ.)**: ^{1}H (399.78 MHz), ^{13}C (100.53 MHz) spectra were recorded on JEOL ECX-400 spectrometer with internal reference signals from residual protic solvent $CHCl_3$ at 7.26 ppm and DMSO-d_6 at 2.50 ppm, along with TMS. As for ^{13}C NMR spectra, the central resonance of the triplet for $CDCl_3$ at 77.16 ppm and the signal for DMSO-d_6 at 39.52 ppm were used as internal references.[1] The resonance multiplicities in the ^{1}H NMR spectra are described as "s" (singlet), "d"(doublet), "t" (triplet), "q" (quartet), "sept" (septet) "m" (multiplet) or "b" (broad). **LC-HRMS (ESI+; Univ. of Strasbourg, CNRS, ISIS, UMR CNRS 7006)**: analyses were performed using a Dionex RSLC U3000HPLC system (Thermo) with a chromatography column Acclaim Phenyl-1, (3µm; 150 x 2.1 mm). The mobile phase was water with 0.1% formic acid (method A) or acetonitrile with 0.1% formic acid (method B). Full MS spectra were acquired using Exactive series 2.9 sp4 software in a positive ion mode at a 3.5 kV spray voltage setting on a Thermo Scientific Exactive Plus EMR. Resolution of full MS and HCD scans were 140000 and data were acquired in profile mode and processed using Xcalibur 4.3. **HRMS (ESI+; Univ. of Bologna, Department of Chemistry)**: HRMS analyses were performed on Waters Xevo G2-XS QTof, ESI+, cone voltage 40 V, capillary 3 kV, source temperature 120 °C. **HPLC** (**Univ. of Bologna, Department of Chemistry**): analysis of the samples content was performed on an Agilent HPLC 1100 coupled with DAD and ESI-MS detectors. A Phenomenex C18 Luna column (3µ Phenyl-Hexyl, 150×4.6mm) was eluted with acetonitrile (ACN) and water (98:2 v/v), flow 1 mL/min at 25°C. UV absorption was monitored at multiple wavelengths (210-420 nm).

Synthesis of 1,2,3,4,5,6-hexakis((4-isopropylphenyl)thio)benzene (**A6-iPr**)

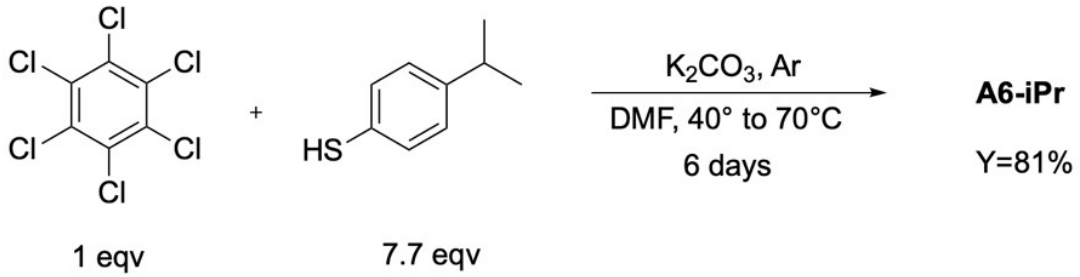

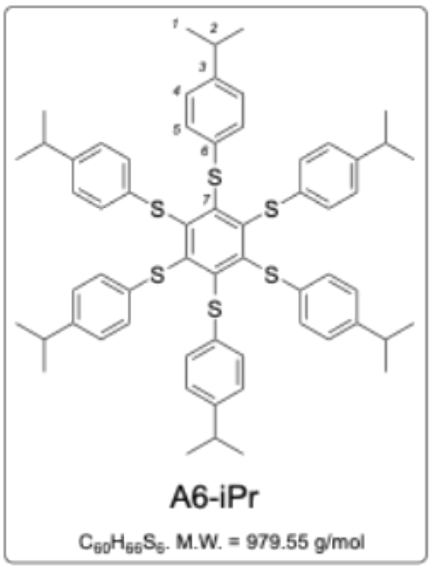

Hexachlorobenzene (0.2510 g, 0.8814 mmol, 1.000 mol-eq) and anhydrous potassium carbonate (0.9325 g, 6.747 mmol, 7.655 mol-eq) are added to an oven-dried reaction tube equipped with a septum. Under argon, dried DMF (6.0 ml) is injected to this tube via a syringe. 4-Isopropylbenzenethiol (1.05 ml, 6,75 mmol, 7.66 mol-eq) is also injected to the reaction mixture under an argon flow. Argon was bubbled through the reaction mixture with a needle for about 5 min. for removing air under vigorous stirring. The tube was sealed with a screw cap and the mixture was vigorously stirred at 40°C for 48 hrs in an oil-bath. The temperature was increased to 70°C for another 96 hrs to complete the process. The tube was then cooled, opened, and a solution (55.0 ml) of ethanol/water (50:50 v/v) was slowly poured into the tube while stirring. A precipitate was formed, collected and dried on a filter. It was transferred to a round-bottom flask equipped with a condenser, and ethanol (95%) was added. The crude solid was triturated with a vigorous stirring in boiling ethanol (20 mL) for about 20 min. Impurities in the supernatant were removed by filtration to collect a pure solid, as monitored by TLC and ^{1}H NMR. A light yellow solid (0.7033 g.; 0.718 mmol; 81% yield) is obtained after drying under vacuum; R_f = 0.34 (toluene/cyclohexane 1:4,v/v). For XRD analysis, hair-like bright yellow crystals were obtained from a slow evaporation of a solution in toluene.

^{1}H NMR (399.78 MHz, $CDCl_3$, ppm): δ = 1.19 (d, *J* = 4.0 Hz, 36H; H1), 2.81 (m, 6H; H2), 6.85 (d_{app}, *J* = 8.0 Hz, 12H; H4), 6.99 (d_{app}, *J* = 8.0 Hz, 12H; H5); **^{13}C NMR** and **^{13}C DEPT135 NMR** (100.53 MHz, $CDCl_3$, ppm): δ = 24.06 (**C**H_3; C1), 33.77 (**C**H$(CH_3)_2$; C2), 127.07 (CH_{arom}; C4), 128.47 (CH_{arom}; C5), 134.96 (C_{arom}; C3), 146.87 (C_{arom}; C6), 148.28 (C_{arom}; C7); **HRMS (ESI+)**: calculated for [$C_{60}H_{66}S_6$ + H^+]: 979.3552 Da, found [M+H^+] 979.3562 m/z.

NMR spectroscopy

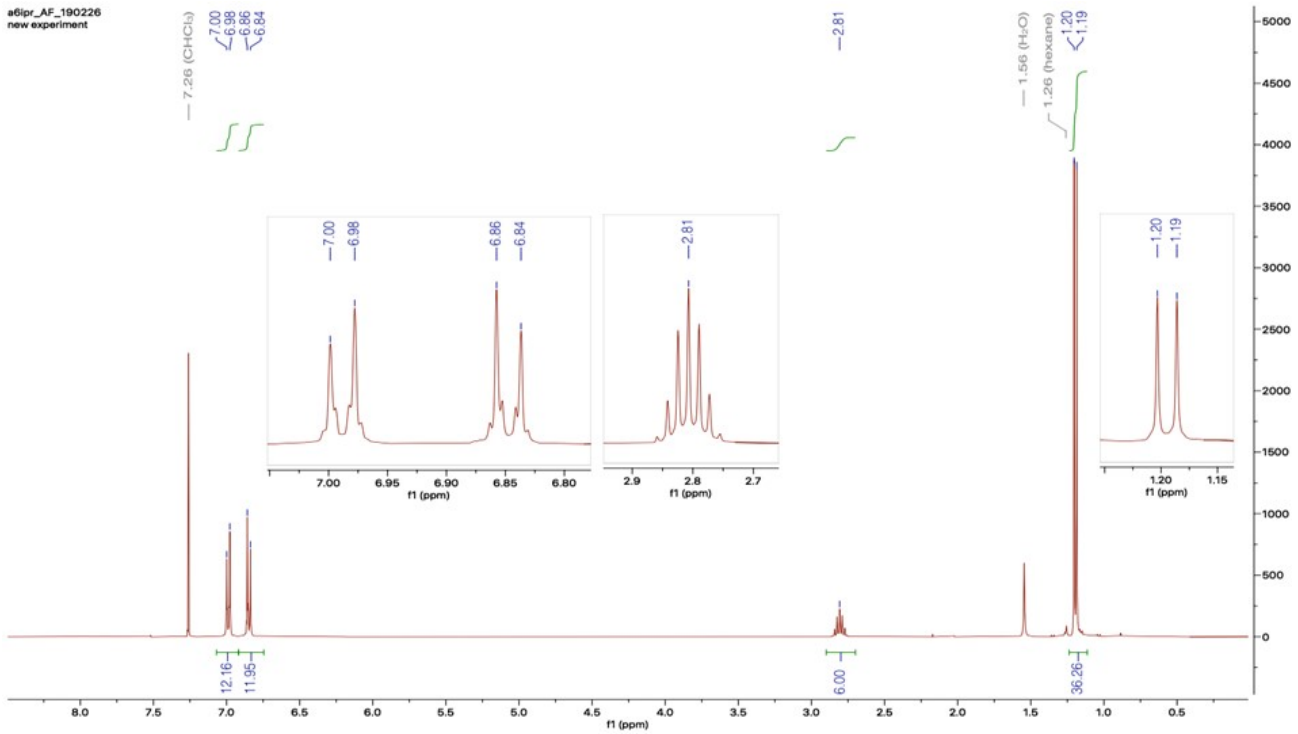

Figure ESI1. ^{1}H NMR of **A6-iPr** (399.78 MHz, $CDCl_3$).

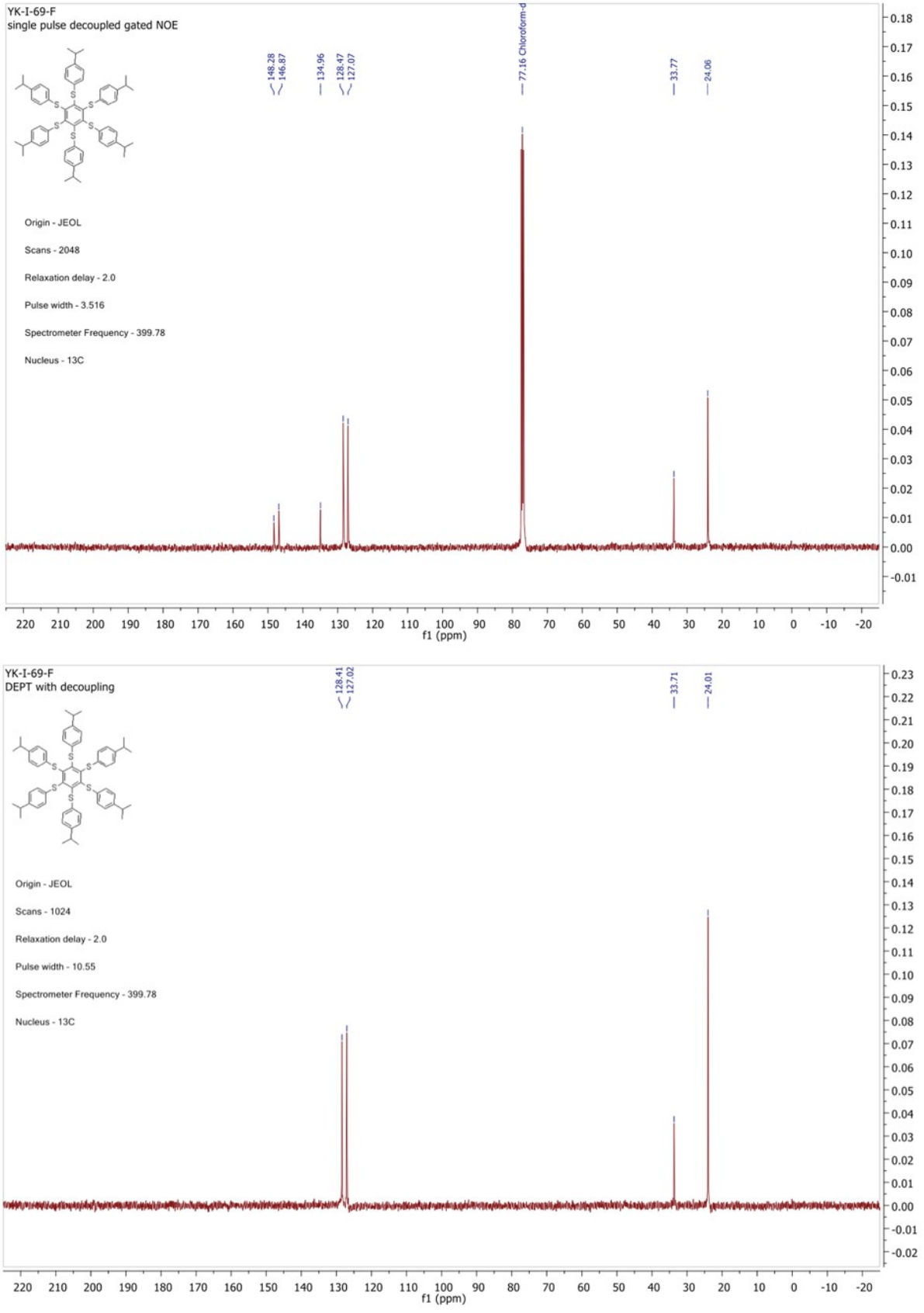

Figure ESI2. ^{13}C-NMR {H} and ^{13}C DEPT NMR spectra of **A6-iPr** ($CDCl_3$, 100.53 MHz).

High-resolution Mass spectrometry (HRMS)

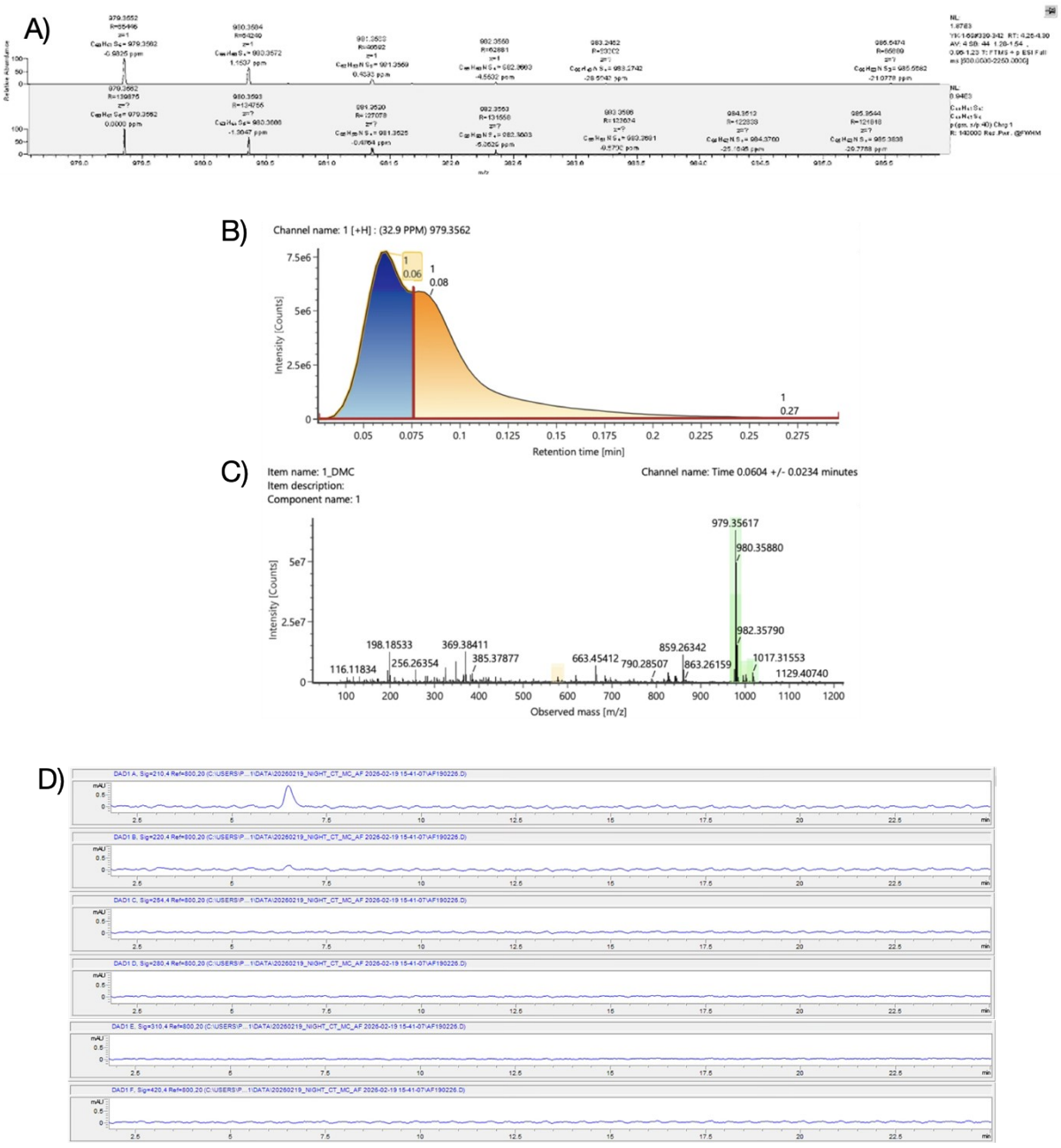

Figure ESI3. A) LC-HRMS spectrum obtained for **A6-iPr**; B) Total ion counting (positive ionisation) and C) corresponding HRMS spectrum for **A6-iPr**. D) HPLC chromatogram for a solution of **A6-iPr** in CH_3CN (retention time = 6.56 min, λ_{abs} = 210-420 nm).

X-Ray Diffraction (XRD) data

Single-crystal XRD data for **A6-iPr** Form I and **A6-iPr** Form II were collected at room temperature (RT) and at low temperature (100K) on an Oxford X'Calibur S CCD diffractometer equipped with a graphite monochromator (Mo Kα radiation, λ = 0.71073 Å). In the case of Form II, all samples showed twinning, and the reflection data were integrated with the default configuration for twinned crystals of the CrysAlisPro Software. The structural solution and refinement were performed using the HKLF4 file containing non-overlapped reflections.

All the structures were solved with SHELXT by intrinsic phasing[2] and refined on F^2 with SHELXL[3] implemented in the OLEX2 software[4] by full-matrix least-squares refinement. H_{CH} atoms for all compounds were added in calculated positions and refined by riding on their respective carbon atoms. All non-hydrogen atoms were anisotropically refined and the rigid-body RIGU restraints[5] applied. Data collection and refinement details are listed in Table ESI1. The Mercury program[6] was used for molecular graphics and calculation of intermolecular interactions. Crystal data can be obtained free of charge via www.ccdc.cam.ac.uk/conts/retrieving.html (or from the Cambridge Crystallographic Data Centre, 12 Union Road, Cambridge CB21EZ, UK; fax: (+44)1223-336-033; or e-mail: deposit@ccdc.cam.ac.uk). CCDC numbers 2522427-2522430.

Phase identification and variable-temperature powder X-ray diffraction measurements were carried out using a PANalytical X'Pert PRO automated diffractometer, which was equipped with an X'Celerator detector in Bragg-Brentano geometry. Cu- Kα radiation (λ = 1.5418 Å) was employed without a monochromator, within a 2θ range of 3° to 40° (continuous scan mode, step size 0.0167°, counting time 1.685 s, soller slit 0.04 rad, antiscatter slit 1/2, divergence slit 1/4, 40 mA 40 kV). An Anton-Paar TTK 450 + LNC was also used. The program Mercury[6] was employed to calculate the powder XRD patterns based on the single-crystal data collected in this study. Hirshfeld surfaces and fingerprint plots for A6-iPr Form I and A6-iPr Form II were generated using crystallographic information files (CIFs) collected at room temperature (RT) in this work, and employing the CrystalExplorer software.[7,8]

In all cases, the identity between polycrystalline samples and single-crystals was always verified by comparing experimental and calculated powder diffraction patterns from this study (Figure ESI7).

Table ESI1. Crystal data and refinement details for **A6-iPr** Form I and **A6-iPr** Form II collected at RT.

	A6-iPr Form I		**A6-iPr Form II**	
Temperature (K)	298	100	298	100
Formula	$C_{60}H_{66}S_6$	$C_{60}H_{66}S_6$	$C_{60}H_{66}S_6$	$C_{60}H_{66}S_6$
FW (g/mol)	979.46	979.46	979.46	979.46
Crystal System	trigonal	trigonal	monoclinic	monoclinic
Space Group	R-3	R-3	$P2_1/c$	$P2_1/c$
a (Å)	22.7937(8)	22.3260(6)	18.861(13)	18.6009(15)
c (Å)	22.7937(8)	22.3260(6)	6.3789(12)	6.3115(4)
c (Å)	9.0138(4)	8.9976(3)	23.076(9)	22.5230(14)
α (°)	90	90	90	90
β (°)	90	90	100.795(6)	100.967(7)
γ (°)	120	120	90	90
Volume (Å^3)	4055.7(3)	3884.0(2)	2727(2)	1.253
Z / Z'	3 / 0.166	3 / 0.166	2 / 0.5	2 / 0.5
ρ_{calc} (g/cm^3)	1.203	1.256	1.193	1.253
μ (mm^{-1})	0.290	0.303	0.288	0.302
Measured Reflections	11135	10277	20474	11936
Independent Reflections	2222	2142	6514	5893
Largest diff. peak/hole (e/Å^3)	0.59/-0.23	0.48/-0.24	0.25/-0.15	0.75/-0.51
R_1	0.0591	0.0482	0.0520	0.0953
wR_2	0.1711	0.1160	0.1304	0.2916

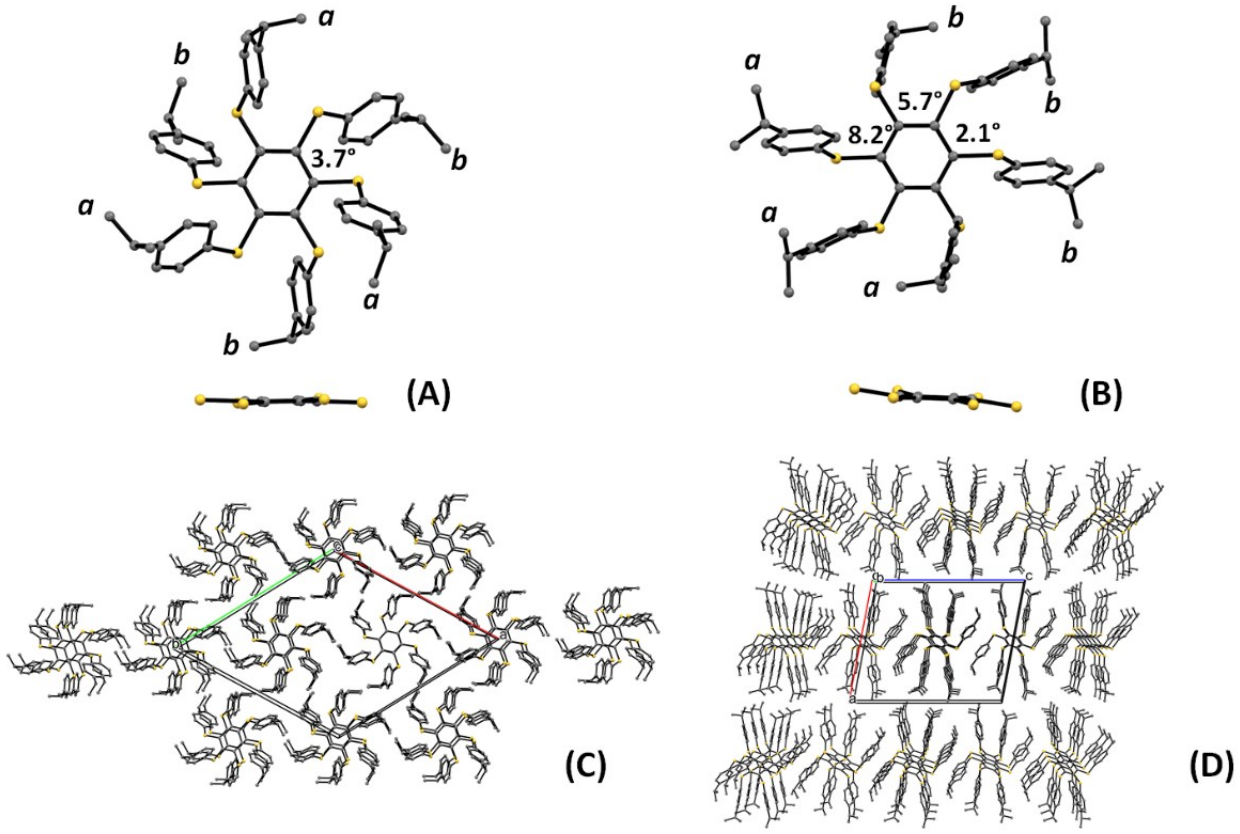

Figure ESI4. Torsional angles in degrees between SC-CS bonds and side views showing the slight differences of the persulfurated benzenes cores detected in crystalline: (A) **A6-iPr** Form I and (B) **A6-iPr** Form II. Crystal packing diagrams for: (C) **A6-iPr** Form I viewed down the c-axis and (D) **A6-iPr** Form II viewed down the b-axis.

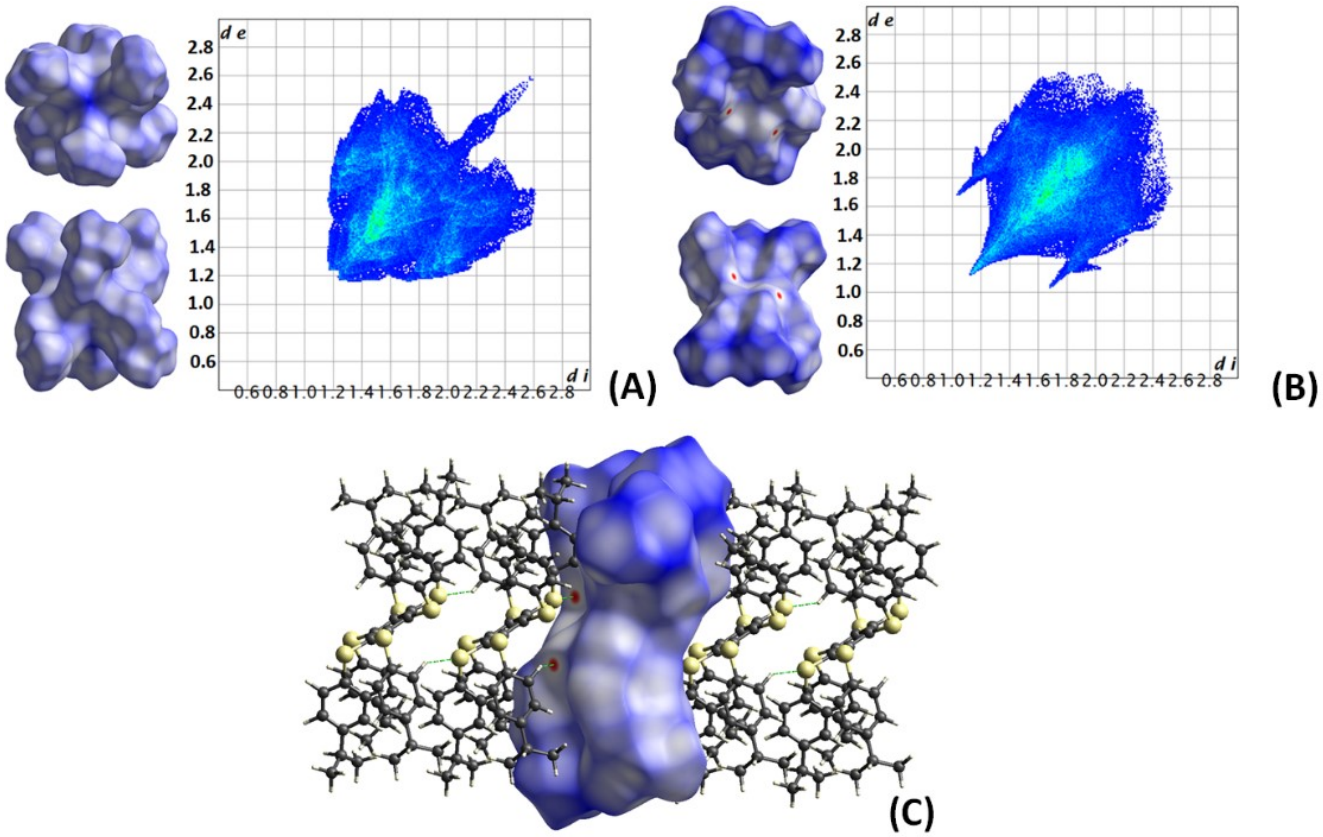

Figure ESI5. Top and side views of the Hirschfeld surfaces mapped with d_{norm} and fingerprint plots of: (A) **A6-iPr** Form I and (B) **A6-iPr** Form II. (C) Close-up view highlighting the weak **C–H···S** interaction [H···S = 2.83(3) Å] between stacked molecules in Form II. Red spots on the d_{norm} surface indicate intermolecular contacts closer than the sum of their van der Waals radii, while longer contacts are in blue, and contacts around the sum of van der Waals radii are in white.

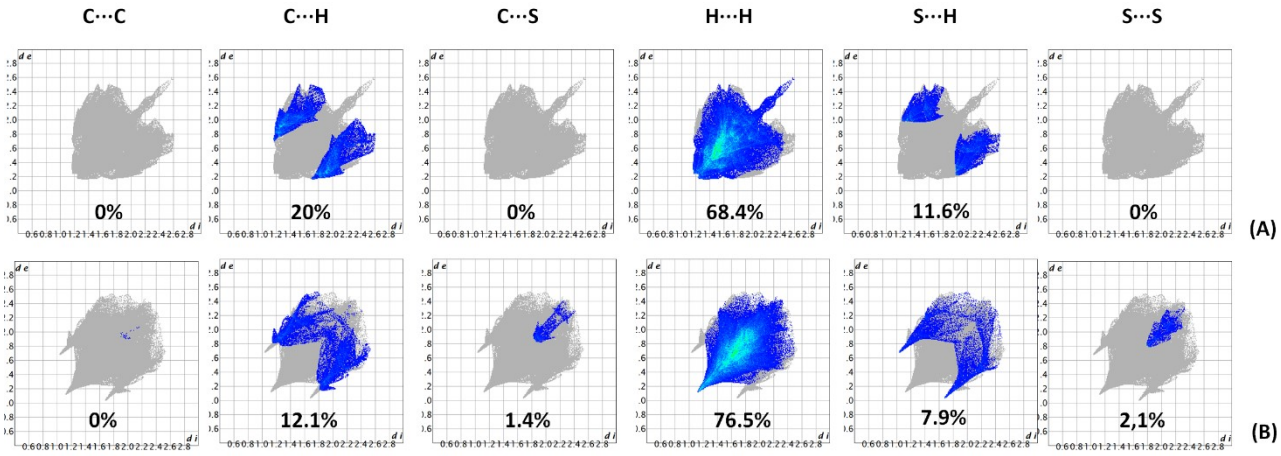

Figure ESI6. Decomposed fingerprint plots showing the relative contributions and percentage contribution of intermolecular contacts in the crystal structures of (A) **A6-iPr** Form I and (B) **A6-iPr** Form II.

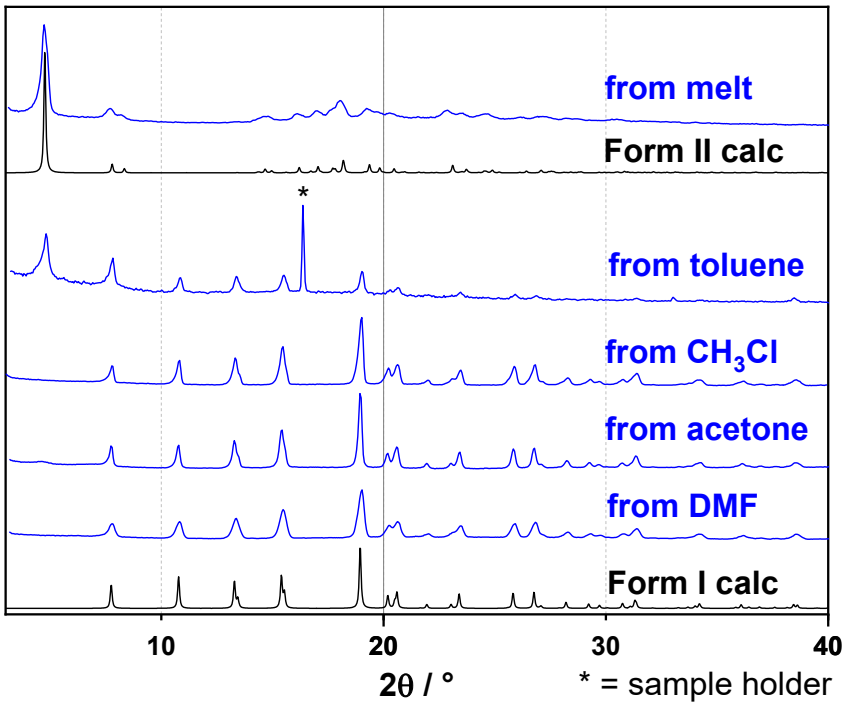

Figure ESI7. Comparison between the experimental (blue line) and calculated (black line) powder XRD patterns for **A6-iPr** Form I (from DMF, acetone, chloroform, and toluene), **A6-iPr** Form II (from the melt) and the mixed phase (from toluene).

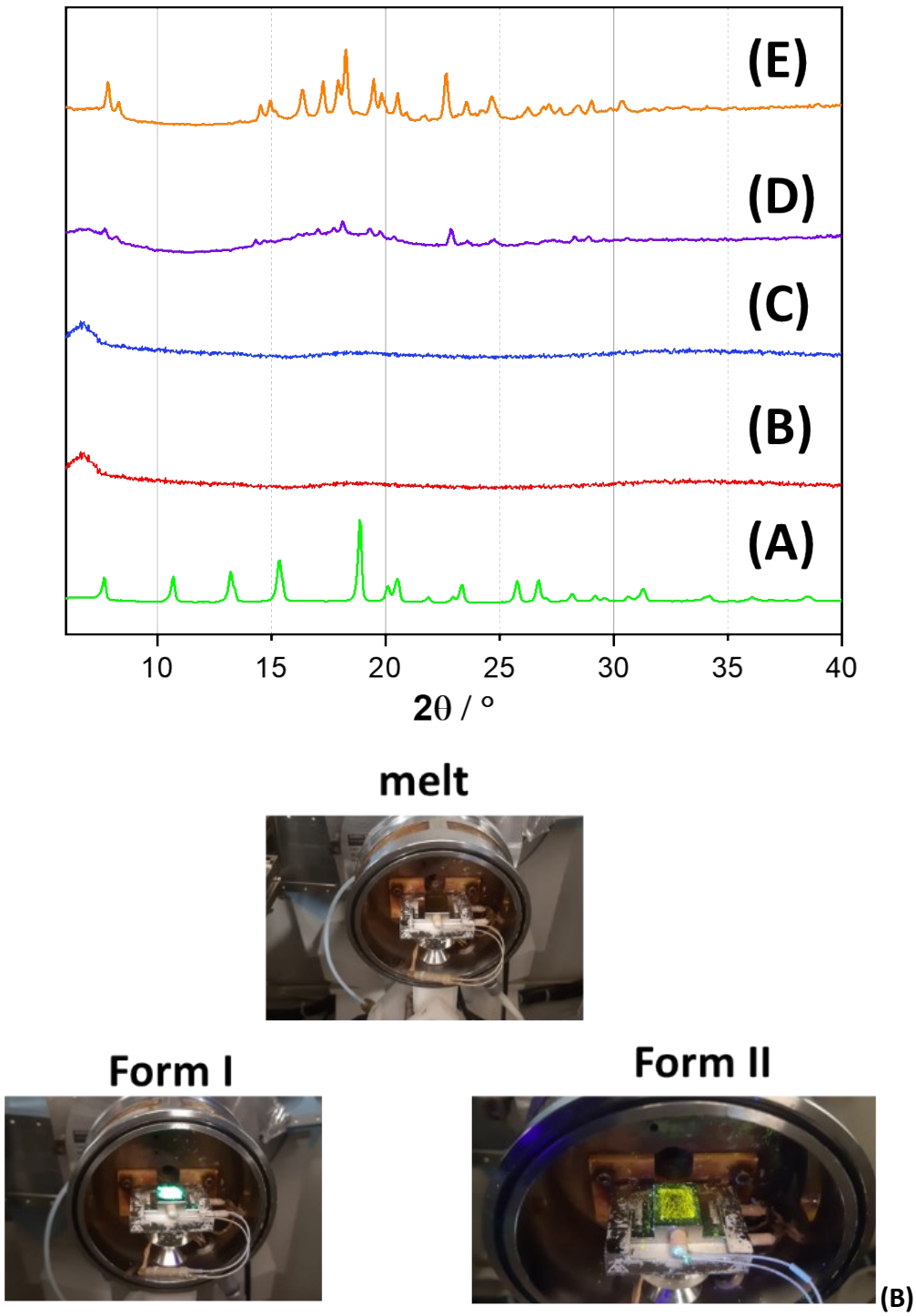

Figure ESI8. Top: VT powder XRD patterns recorded at different temperatures showing the interconversion of a polycrystalline sample of **A6-iPr** Form I into Form II via formation of an amorphous phase: (A) form I at RT, (B) the melt phase at 200°C, (C) the amorphous phase at RT, (D) recrystallization of Form II at 80°C, and (E) Form II at 100°C. Bottom: Photographs taken under UV irradiation during the interconversion of **A6-iPr** Form I into Form II, via the formation of a melt/amorphous phase as monitored by VTPXRD.

Intermolecular Interaction Energies (IIEs)

Interaction energies (IIEs),[9] resulting from the sum of electrostatic, polarization, dispersion and repulsion contributions, were evaluated with the help of the program Crystal Explorer[7,10] from the crystallographic information files (CIF) collected in this work. IIEs between pairs of molecules are indicated by the same color in Table SI2 and in the corresponding Figure S5.

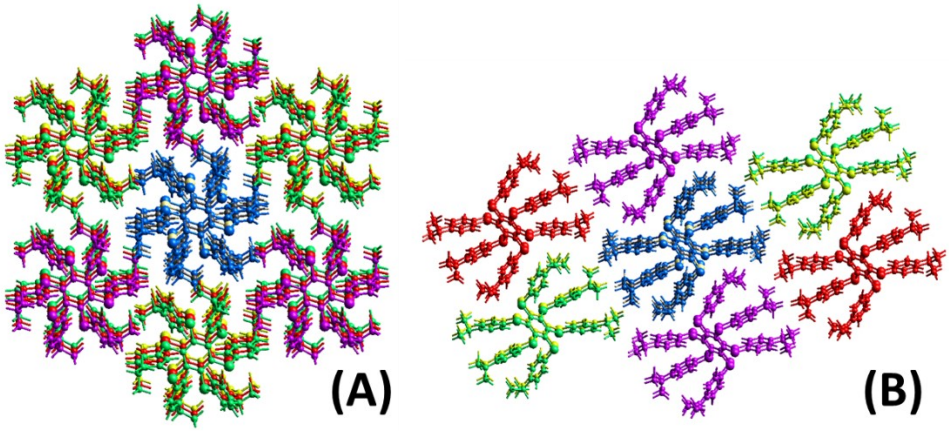

Figure ESI9. Pairs of interacting molecules that contribute most to the total interaction energy in crystalline **A6-iPr** Form I (A) and **A6-iPr** Form I (B).

Table ESI2. Electrostatic, polarization, dispersion, repulsion terms and total interaction energy within the pairs of molecules shown in Figure S5. Evaluated with the Crystal Explorer Package and using the CE-B3LYP/631G(d,p) (k_ele = 1.019; k_pol = 0.651; k_disp =0.901; k_rep = 0.811) as energy model and basis set.

		R (Å)[a]	$E_{ele.}$ (kJ/mol)	$E_{pol.}$(kJ/mol)	$E_{disp.}$(kJ/mol)	$E_{rep.}$(kJ/mol)	$E_{tot.}$(kJ/mol)
A6-iPr Form I		14.47	-4.3	-1.1	-40.8	17.5	-30.1
		19.96	-0.3	0.0	-5.0	1.1	-4.0
		13.50	-1.5	-0.3	-30.	11.5	-20.9
		9.00	-27.1	-9.5	-190.3	103.4	-137.6
		19.96	-0.3	0	-5.0	1.1	-4.0
A6-iPr Form I I		20.41	-0.7	-0.1	-7.0	0.0	-6.9
		18.86	2.2	-0.1	-22.3	0.0	-17.1
		19.91	1.6	-0.1	-14.7	0.0	-11.1
		6.37	-34.3	-5.5	-178.9	119.5	-122.4
		11.97	-10.4	-2.4	-64.1	33.0	-48.2

[a]= distance between molecular centroids (mean atomic positions).

Thermogravimetric Analysis (TGA)

TGA analyses were performed with a PerkinElmer TGA 8000. Each sample contained in a platinum crucible, was heated in a nitrogen flow (20 $cm^3 \cdot min^{-1}$) at a rate of 5 $°C \cdot min^{-1}$; up to decomposition. Samples weights were in the range 5-10 mg.

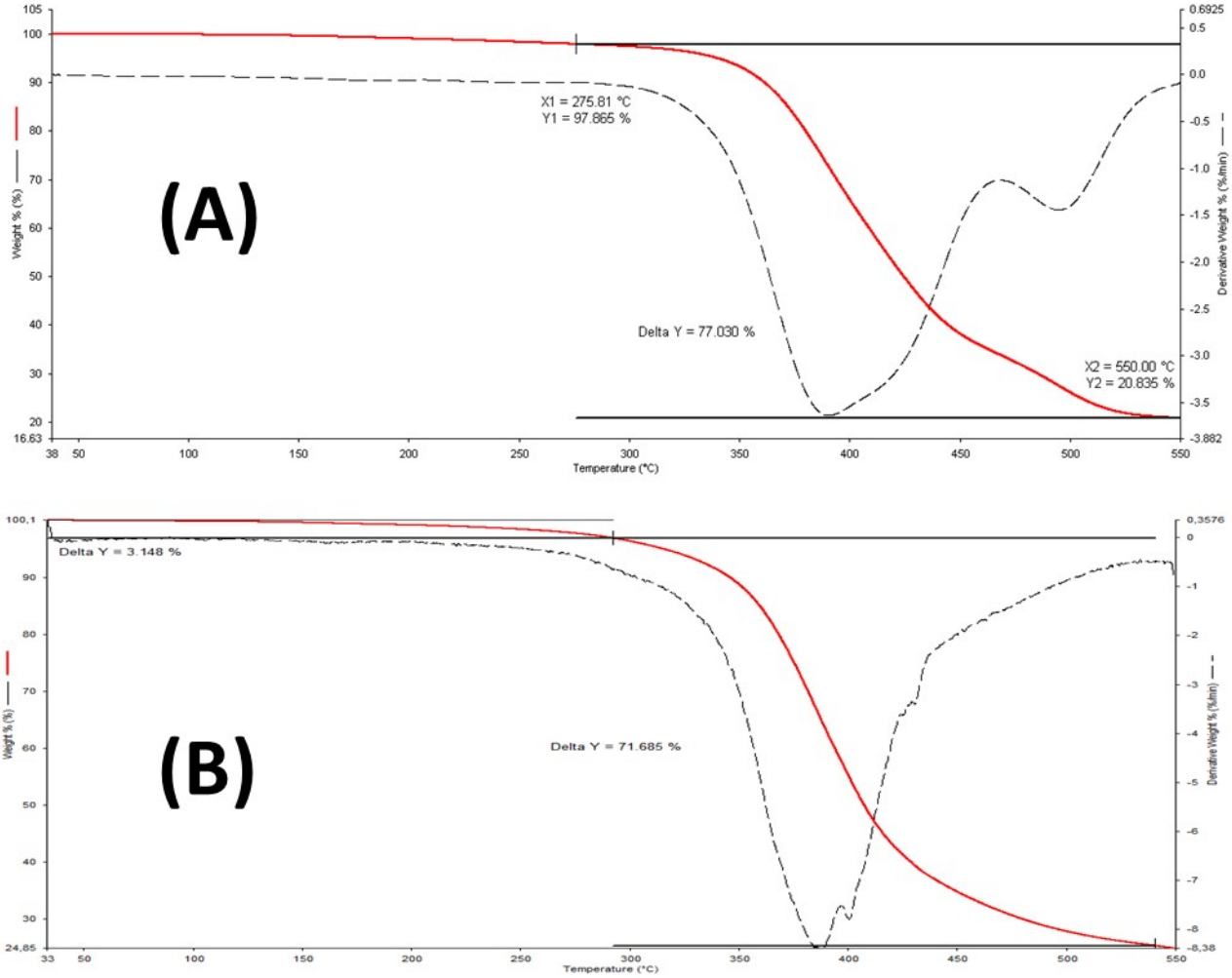

Figure ESI10. Thermograms of polycrystalline **A6-iPr**: (A) Form I and (B) Form II. Red lines represent weight losses, and black dashed lines represent the corresponding derivatives.

Differential Scanning Calorimetry (DSC)

Calorimetric measurements were performed with a PerkinElmer DSC-7 equipped with a PII intracooler. Temperature and enthalpy calibrations were performed high-purity standards (n-decane, benzene, and indium). Heating of the aluminium open pans containing the samples (3-5 mg) was carried out at 5 °C·min-1 in the temperature range 20 – 120°C under N_2 atmosphere.

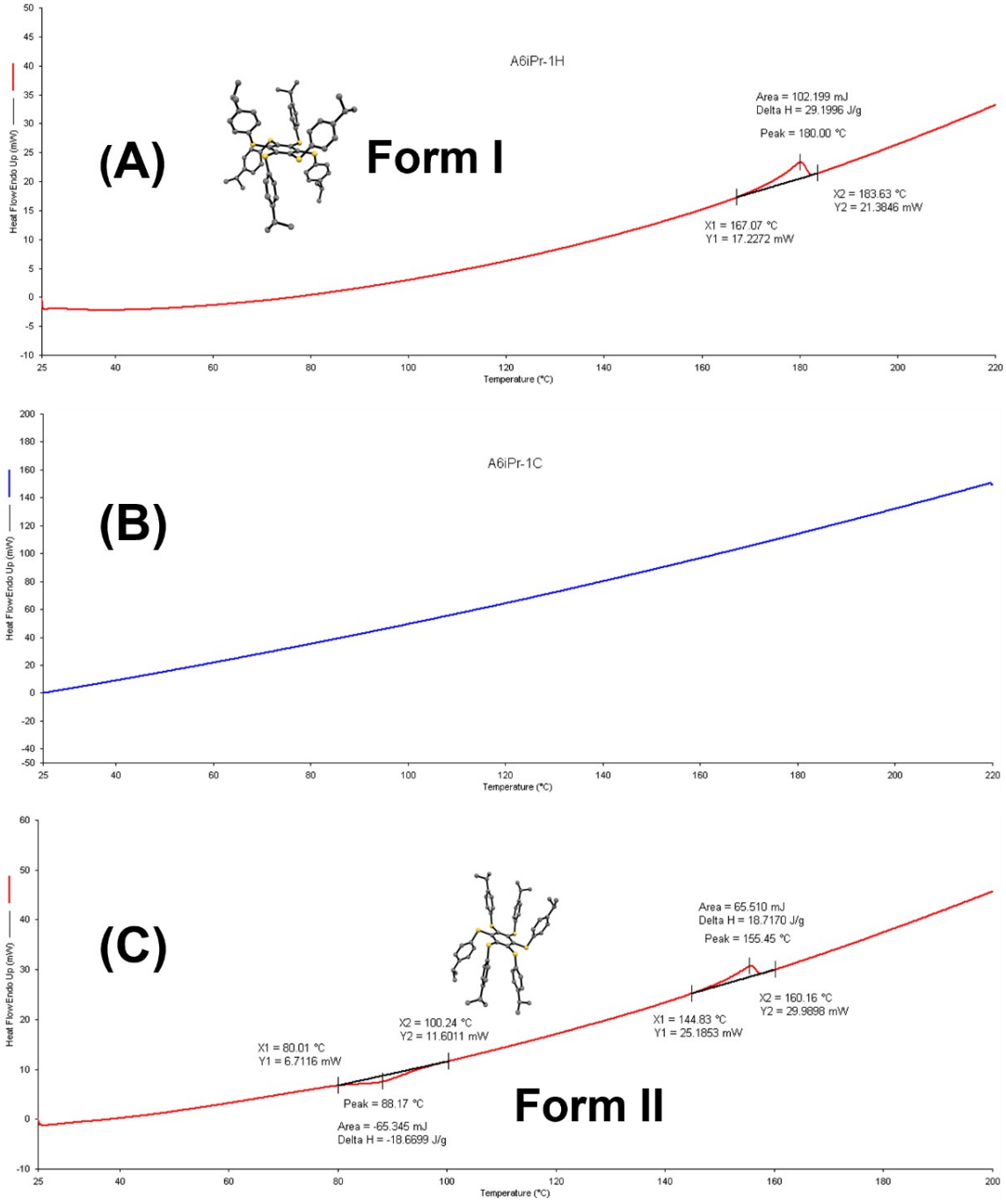

Figure ESI11. DSC traces of polycrystalline **A6-iPr**: (A) first heating, showing the melting of Form I; (B) first cooling; and (C) second heating, showing crystallization into Form II followed by its melting.

Photophysical characterization

General information: all photophysical analyses were carried out on solid samples or in CH_2Cl_2 solutions, unless otherwise specified. Amorphous samples have been prepared by melting powders or crystals in a glass pipette and quickly freezing them in liquid nitrogen. UV–vis absorption spectra were recorded with a Agilent Cary 300 spectrophotometer using quartz cells with path length of 1.0 cm. Reflectance spectra were recorded with a Perkin Elmer 365+, equipped with an integrating sphere, on dispersions of the solid compounds in dried $BaSO_4$ (ca. 1% w/w). Luminescence spectra and lifetimes were recorded on a PerkinElmer LS-50, a Edinburgh FS5, a Edinburgh FLS920 (equipped with a Hamamatsu Photomultiplier R928P phototube) or on a Varian Cary Eclipse spectrofluorometer. Lifetimes shorter than 10 µs were measured by the same Edinburgh FLS920 spectrofluorometer by time-correlated single-photon counting (TCSPC) technique. Quantum yields of solid samples are determined by means of an integrating sphere (LabSphere, 4 in. diameter) with the method developed by De Mello.[11] Quantum yields of solutions at 77 K were calculated with the same apparatus using an homemade optical glass dewar flask, vertically fitting the above-mentioned integrating sphere. The estimated experimental errors are 2 nm on the band maximum, 5% on the molar absorption coefficient and luminescence lifetime and 20% on emission quantum yields.

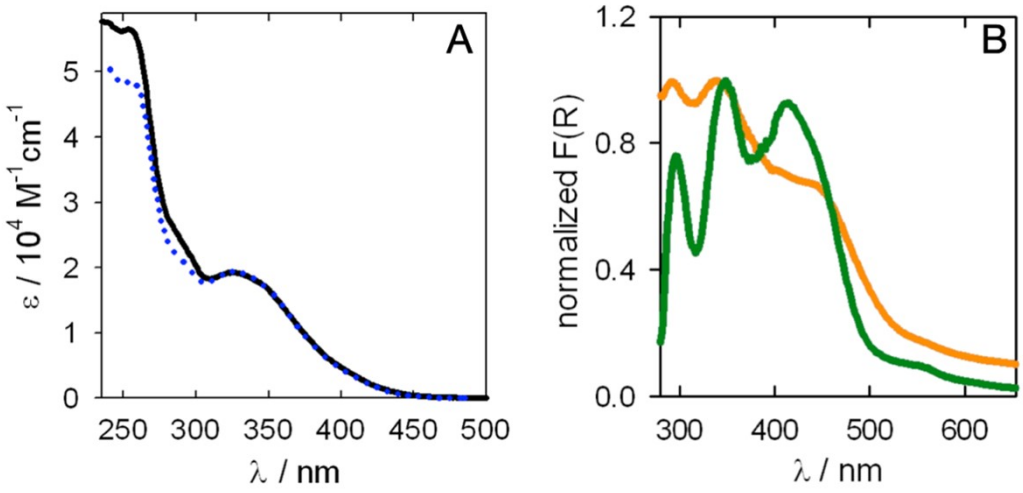

Figure ESI12. A: comparison between absorption spectra in CH_2Cl_2 solutions at RT for **A6-iPr** (black) and its methylated analogue (1,2,3,4,5,6-hexakis(*p*-tolylthio)benzene; data from reference n° [12]). B: Kubelka-Munk function (F(R) calculated for solid **A6-iPr**; Forms I and II, green and orange lines, respectively) at RT from diffuse reflectance spectra in $BaSO_4$ matrices (ca. 1% w/w), according to $F(R)=(1-R)^2/2R$.

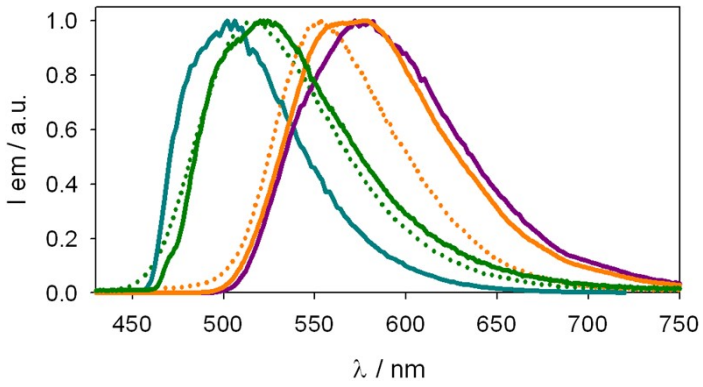

Figure ES13. Comparison between emission spectra collected for the two polymorphs of **A6-iPr** at 77 K (Form I: green line; Form II: orange line). The corresponding emissions at RT are shown for comparison as dotted lines. The emission spectrum obtained from frozen diluted solutions in CH_2Cl_2:CH_3OH (1:1, v/v) is shown as the blue line. The emission spectrum obtained from the amorphous phase at 77 K is shown as the purple line. λ_{ex} = 350 nm.

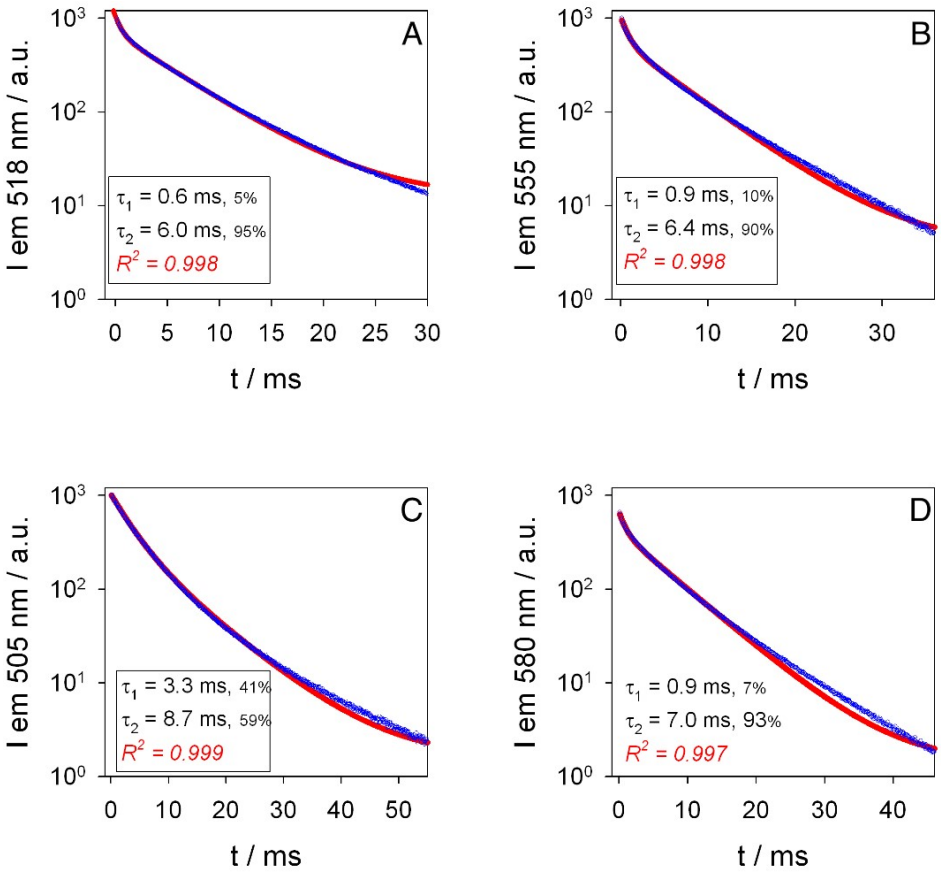

Figure ESI14. Emission decays at emission maxima for **A6-iPr** in different experimental conditions at 77 K: A) Form I, solid; B) Form II, solid; C) diluted rigid matrix in CH_2Cl_2:CH_3OH (1:1, v/v); D) amorphous phase, solid. The biexponential fitting functions are also shown as red lines.

Table ESI3. Photophysical parameters of solid phases at low temperature

	Emission at 77 K		
	λ_{max} (nm)	τ (ms)	Φ
A6-*i*Pr (Form I)	520	0.6 - 6.0 [a]	0.4
A6-*i*Pr (Form II)	554	0.9 - 6.4 [a]	0.13
A6-*i*Pr (amorphous solid)	576	0.9 - 7.0 [a]	0.6
A6-*i*Pr (diluted rigid matrix)	502	3.3 - 8.7 [a]	0.5

[a] Biexponential fitting.

Computational Details

Quantum-chemical (QC) calculations were carried out on the two conformers of **A6**-**IPr,** *ababab* and *aaabbb* forming the two polymorphs to investigate their optical properties. To this end, ground and excited state geometries were optimized. Both isolated molecules and condensed phases were investigated. The optimized ground state geometries of **A6**-**iPr** were determined at M06-2X/def2-SVP level of theory including the D3 version of Grimme's dispersion.[13] Vertical excitations energies were evaluated at TD-M06-2X level with the same basis set and D3 dispersion. Excited state geometries were obtained at TD-M06-2X-D3/def2-SVP level or with UM06-2X-D3/def2-SVP. The M06-2X functional was considered due to its closer agreement with experimental data.

To assess the role of intermolecular interactions, excited state calculations at TD-M06-2X/def2-SVP+D3 level were carried out on model aggregates (dimers and trimers) of **A6**-**iPr**. We also investigated the crystal environment with QM/MM calculations. QM/MM calculations were performed with the Gaussian16 package[14] and the ONIOM model,[15] using the M06-2X functional and def2-SVP basis set for the high-level region (i.e. a central **A6**-**iPr** molecule) and the QM calculations included electronic embedding. The low-level region (molecular mechanics) was modelled by atomic point charges determined by the charge equilibration (Qeq) approach[16] using the Dreiding force field[17] parameters attributed to the fixed molecular geometry of the surrounding **A6**-**iPr** molecules.

A 3𝒂3𝒂5 supercell including 170 **A6**-**iPr** molecules was used for polymorph Form I while a 5𝒂5𝒂2 supercell including 140 **A6**-**iPr** molecules was used for polymorph Form II. The ground state geometry of the central molecule was optimized with QM/MM calculations and excitation energies were determined with QM/MM calculations. In addition, also the geometry of the lowest triplet state was optimized by QM/MM calculations. All the QC calculations were carried out with the Gaussian16 package.[12]

Table ESI4. Computed vertical excitation energies (eV) at the optimized ground state geometry of the two **A6-iPr** conformers. From TD-M06-2X-D3/def2-SVP calculations for isolated molecules and TD-M06-2X-D3/def2-SVP level for the QM part of the QM/MM calculations describing crystal embedding.

Conformer	**$S_0 \rightarrow T_1$** / eV Isolated [crystal]	**$S_0 \rightarrow T_2$** / eV Isolated [crystal]	**$S_0 \rightarrow T_3$** / eV Isolated [crystal]
A6-iPr-*ababab*	3.30 (ππ*)[a] [3.16] (nπ*/ππ*)[b]	3.54 [3.47]	3.54 [3.47]
A6-iPr-*aaabbb*	3.01 (nπ*/ππ*)[a] [2.93] (nπ*/ππ*)[b]	3.22 [3.16]	3.63 [3.65]

[a] Dominant orbital character of the T_1 excited state in gas-phase. [b] Dominant orbital character of the T_1 excited state with crystal embedding via QM/MM calculations.

Table ESI5. Effect of crystal embedding on optimized T_1 geometries and vertical emission energies (eV) for the two **A6-iPr** conformers. Vertical emission energies computed at TD-M06-2X-D3/def2-SVP level for isolated molecules and TD-M06-2X/def2-SVP level for the QM part of QM/MM calculations to model crystal embedding effects.

Conformer	**$T_1 \rightarrow S_0$** (gas phase) / eV **@ T_1** geo gas phase	**$T_1 \rightarrow S_0$** (gas phase) / eV **@ T_1** geo QM/MM	**$T_1 \rightarrow S_0$** (QM/MM) / eV **@ T_1** geo QM/MM	**Exp**[a] / eV
A6-iPr-*ababab*	1.70	2.68	2.68	2.39
A6-iPr-*aaabbb*	2.35	2.26	2.28	2.24

[a] Solid state emission, RT, see Table 2.

Table ESI6. Comparison of TD-M06-2X-D3/def2-SVP computed vertical excitation energies (*E* / eV) for the lowest triplet excited states of a single **A6-iPr** molecule, *aaabbb* conformer, and for a dimer and trimer of the same molecule, as extracted from the crystal structure (see Figure ESI22 and ESI23).

Excited state	**Monomer** ***E*** / eV	**Dimer** ***E*** / eV	**Trimer** ***E*** / eV
T_1	2.96	2.97-2.97	2.97-2.97-2.98
T_2	3.08	3.11-3.11	3.11-3.11-3.13
T_3	3.66	3.68-3.68	3.68-3.68-3.70

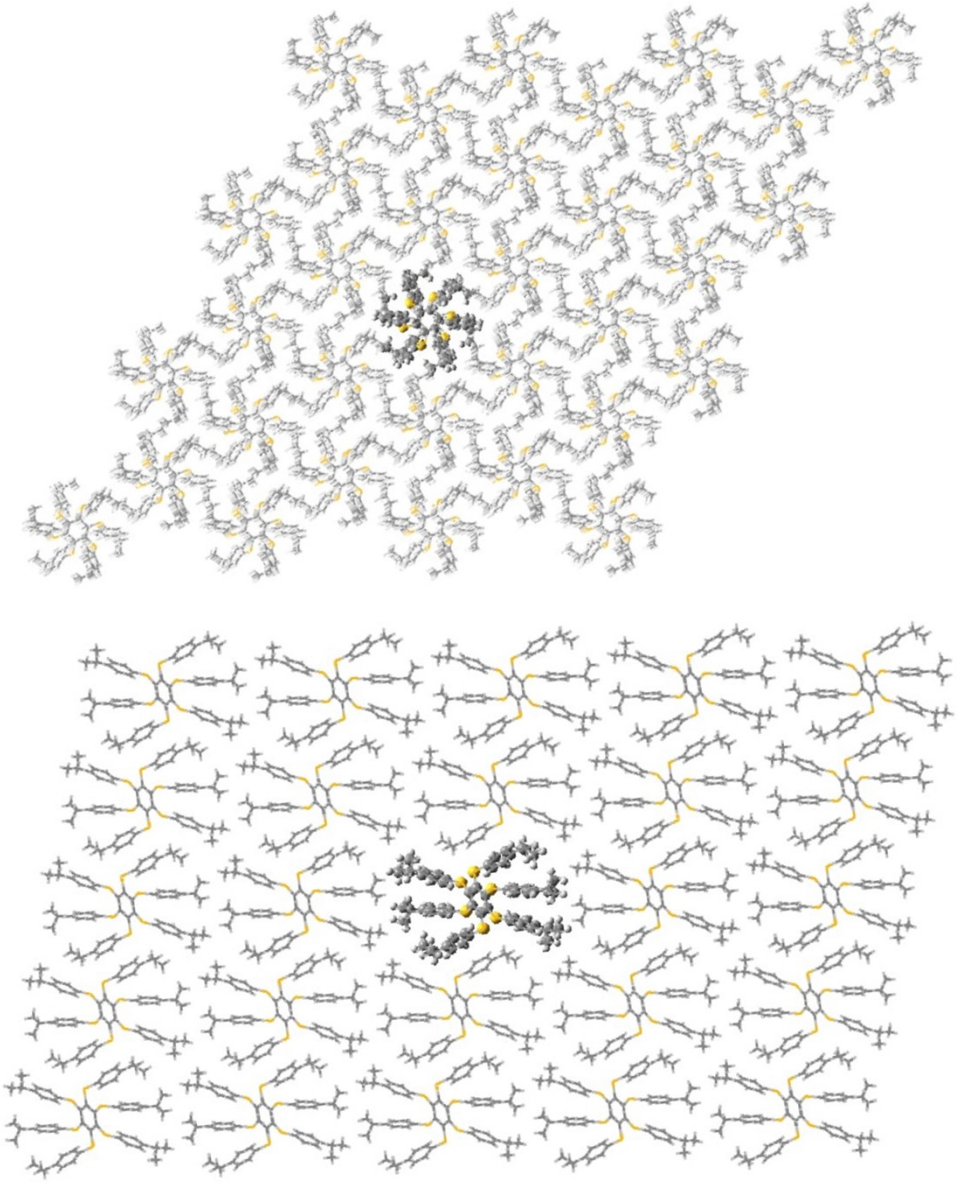

Figure ESI15. Supercell used in QM/MM calculations: (top) **A6-iPr**, *ababab* conformer, 3𝒾3𝒾5 supercell, (bottom) **A6-iPr**, *aaabbb* conformer, 5𝒾5𝒾2 supercell. The molecule described at QM level in QM/MM calculations is highlighted in ball and stick representation.

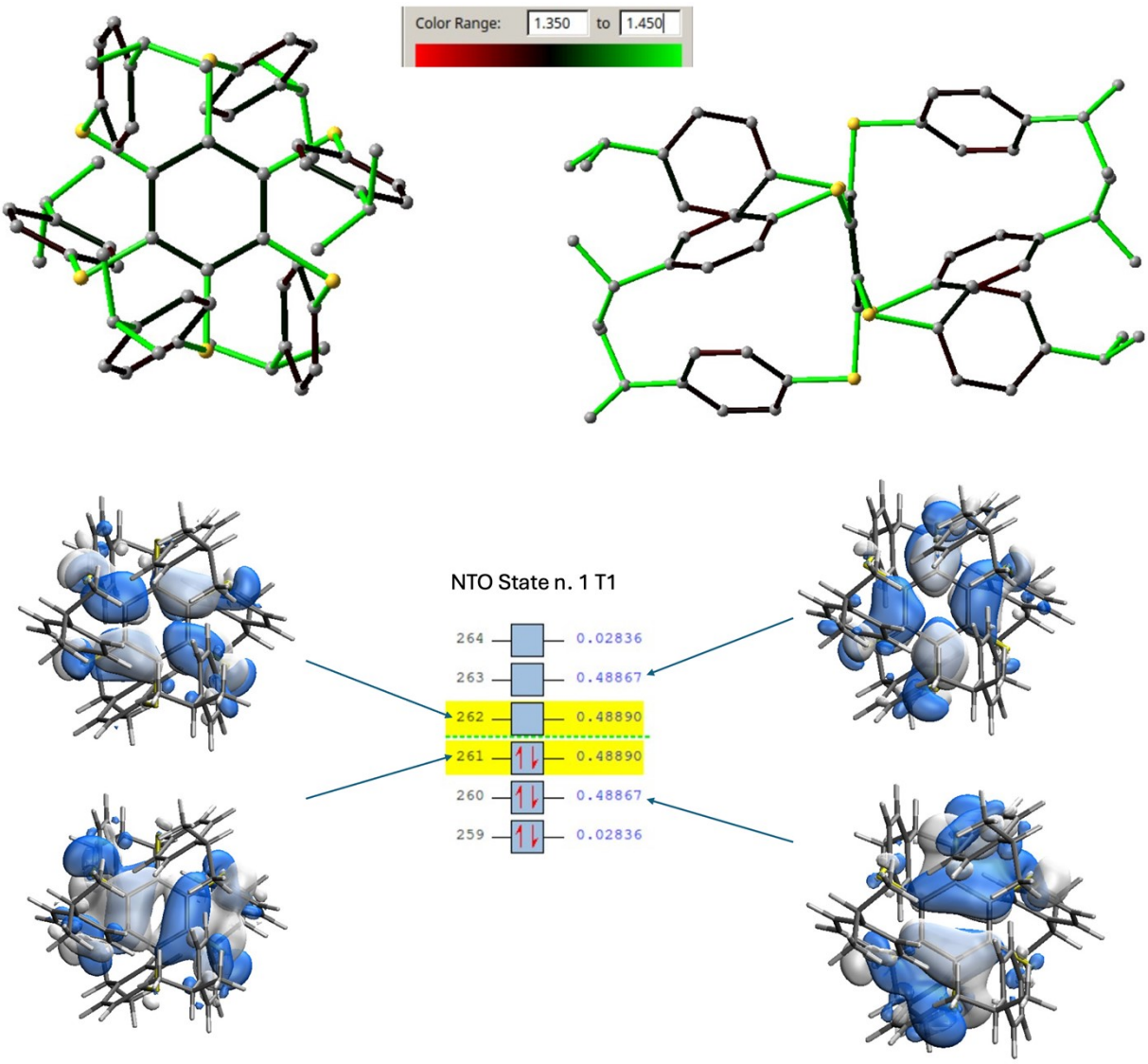

Figure ESI16. A6-iPr, *ababab* conformer (Form I): (top) Gas-phase optimized ground state geometry (M06-2X-D3/def2-SVP), hydrogen atoms not shown, color range for bond lengths shown in the inset: aromatic rings appear as dark-grey, markedly double bonds appear in red, longer bonds in green; (bottom) NTO analysis of the lowest triplet excited state showing dominant ππ* character (TD-M06-2X-D3/def2-SVP, see Table ESI4).

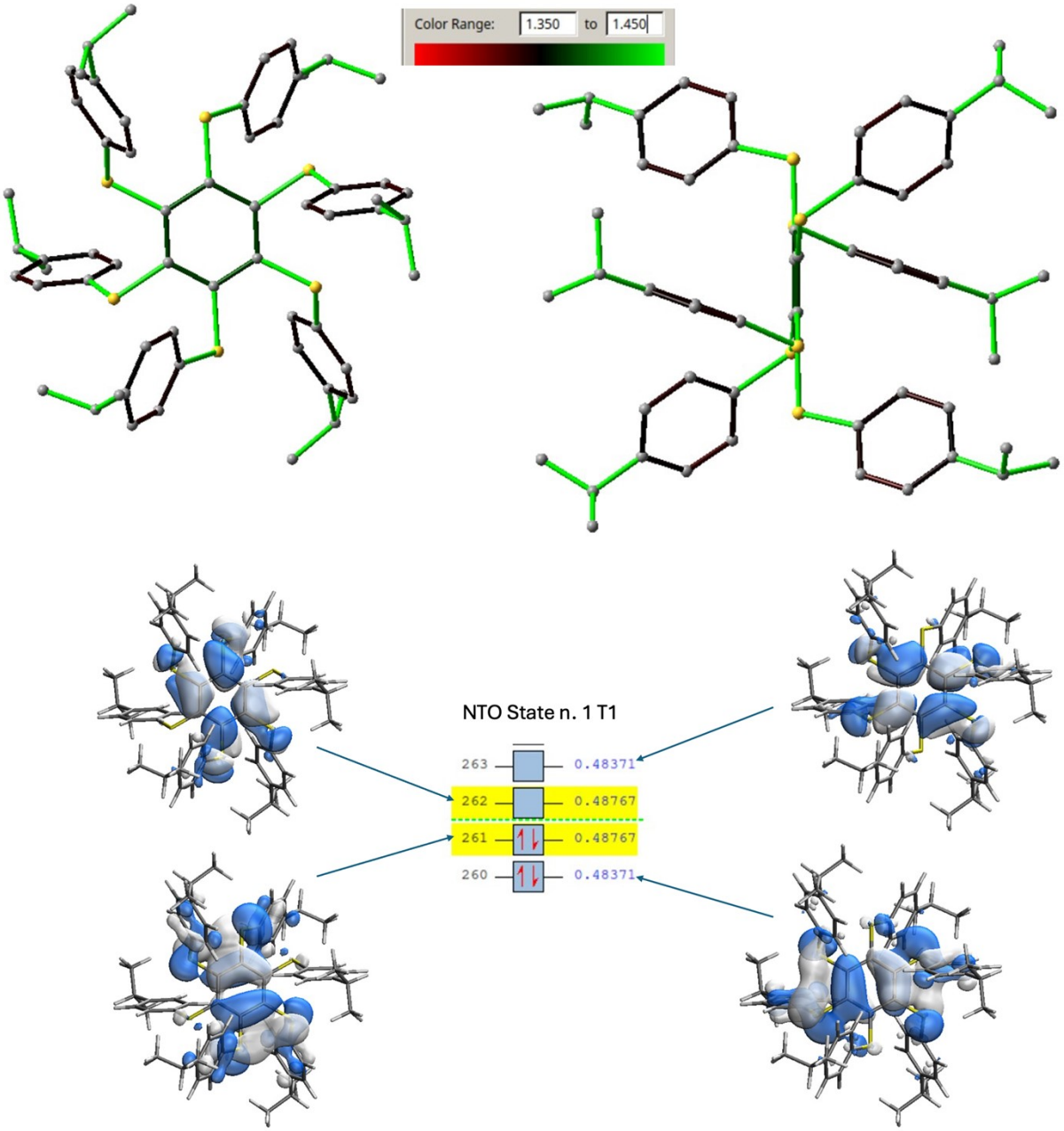

Figure ESI17. A6-iPr, *ababab* conformer (Form I): (top) QM/MM optimized ground state geometry (embedded in the crystal) (M06-2X-D3/def2-SVP), hydrogen atoms not shown, color range for bond lengths shown in the inset: aromatic rings appear as dark-grey, markedly double bonds appear in red, longer bonds in green; (bottom) NTO analysis of the lowest triplet excited state showing mixed ππ*/nπ* character (TD-M06-2X-D3/def2-SVP, see Table ESI4).

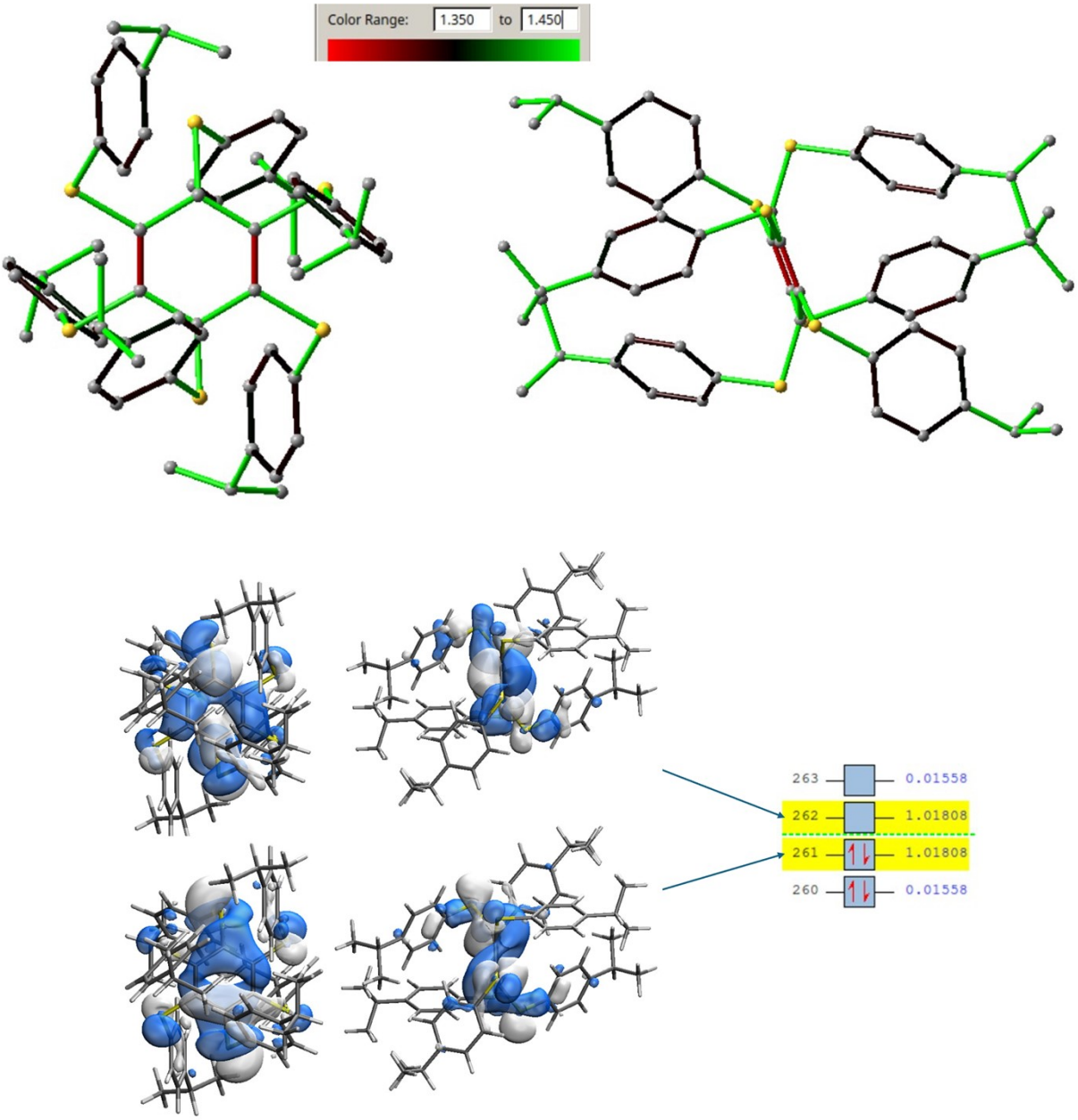

Figure ESI18. A6-iPr, *ababab* conformer (Form I): (top) Gas-phase optimized T_1 state geometry (TD-M06-2X-D3/def2-SVP), hydrogen atoms not shown, color range for bond lengths shown in the inset: aromatic rings appear as dark-grey, markedly double bonds appear in red, longer bonds in green. The quinoidal structure of the central ring is clearly seen, due to the localized excitation; (bottom) NTO analysis of the lowest triplet excited state showing front and side views of HONTO and LUNTO (TD-M06-2X-D3/def2-SVP).

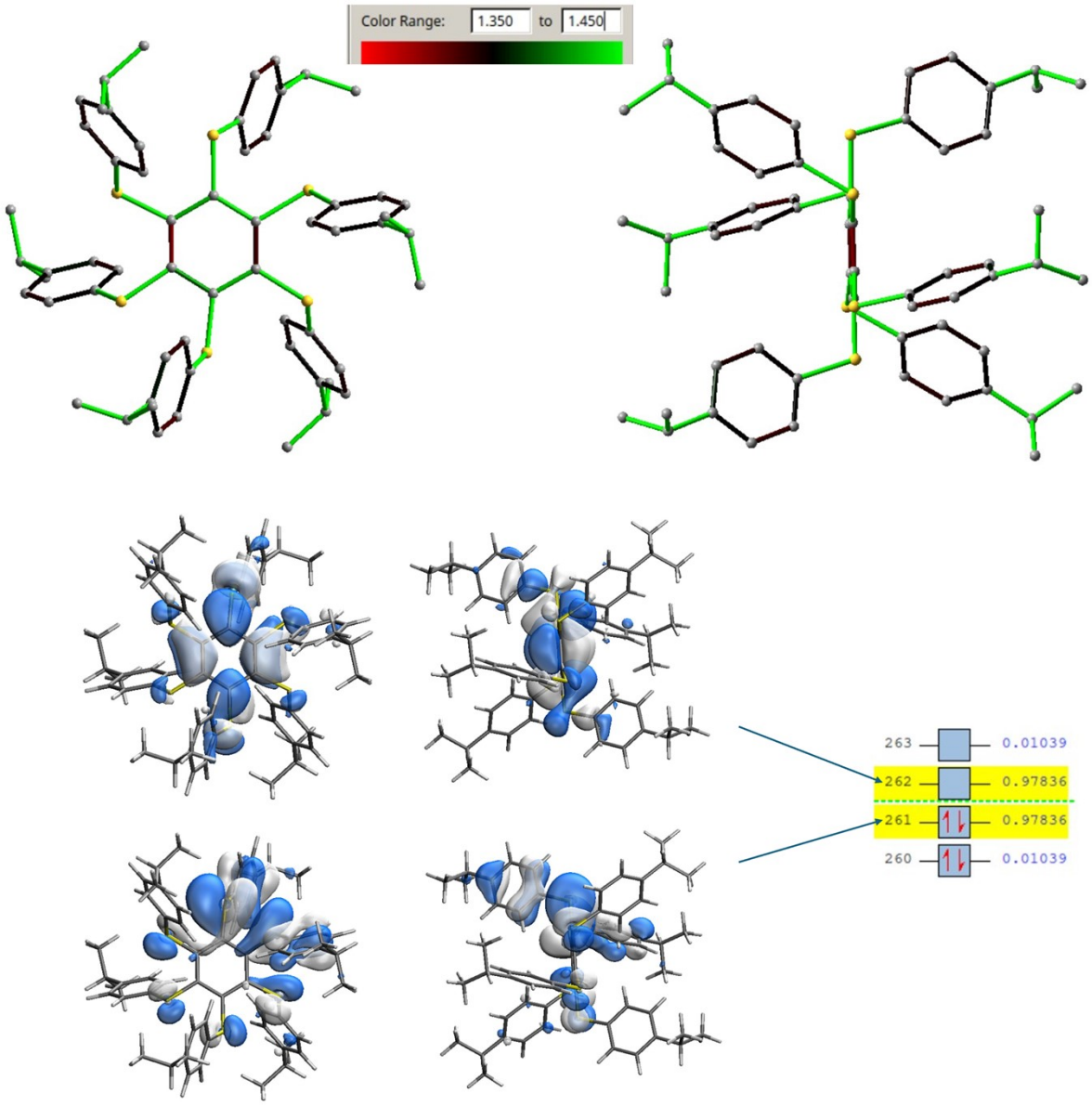

Figure ESI19. A6-iPr, *ababab* conformer (Form I): (top) QM/MM optimized T_1 state geometry (embedded in the crystal) (UM06-2X-D3/def2-SVP), hydrogen atoms not shown, color range for bond lengths shown in the inset: aromatic rings appear as dark-grey, markedly double bonds appear in red, longer bonds in green. The quinoidal structure of the central ring is clearly seen, due to the localized excitation; (bottom) NTO analysis of the lowest triplet excited state showing front and views of HONTO and LUNTO (TD-M06-2X-D3/def2-SVP).

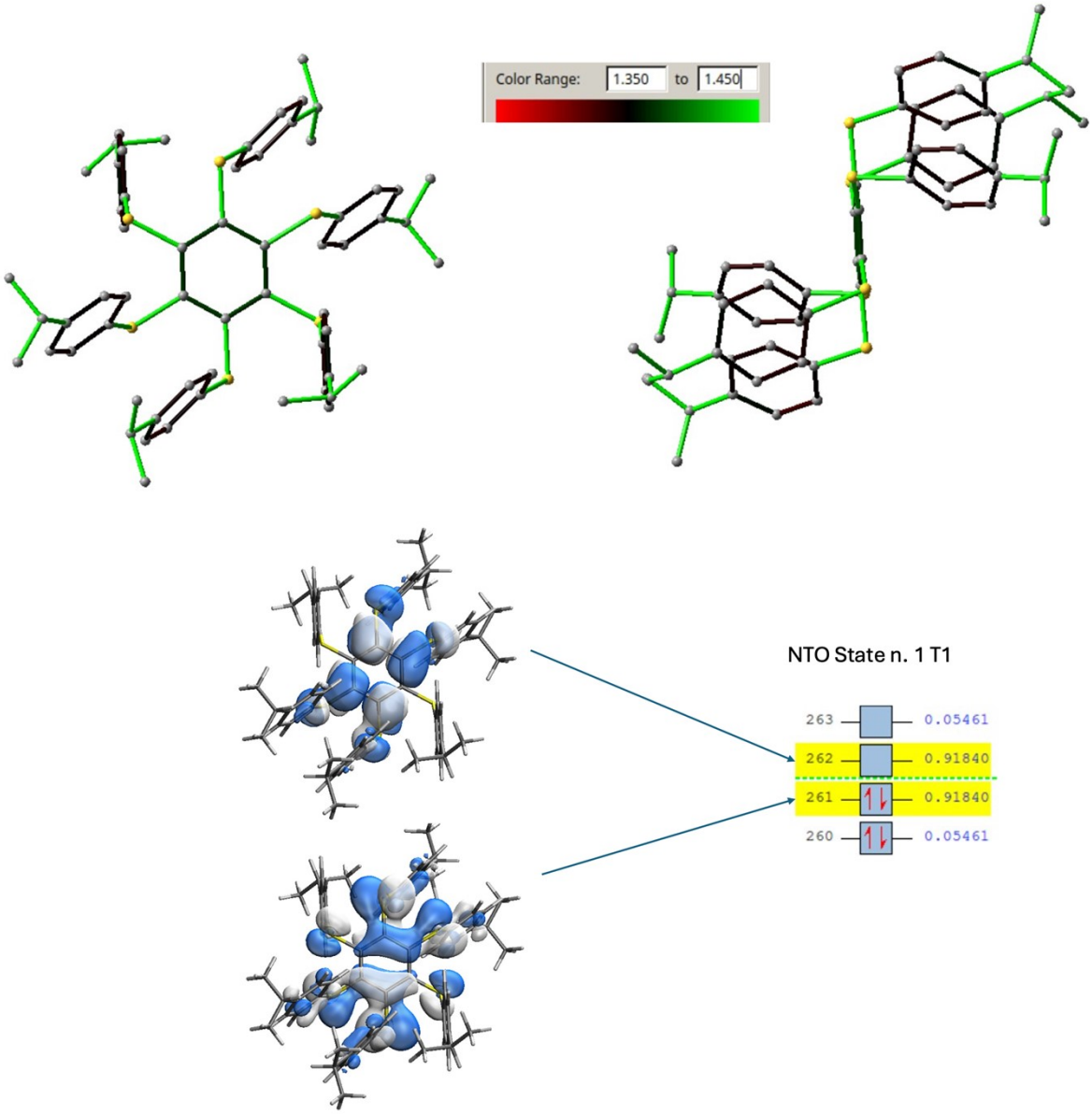

Figure ESI20. A6-iPr, *aaabbb* conformer (Form II): (top) Gas-phase optimized ground state geometry (M06-2X-D3/def2-SVP), hydrogen atoms not shown, color range for bond lengths shown in the inset: aromatic rings appear as dark-grey, markedly double bonds appear in red, longer bonds in green; (bottom) NTO analysis of the lowest triplet excited state showing mixed ππ*/nπ* character (TD-M06-2X-D3/def2-SVP, see Table ESI4).

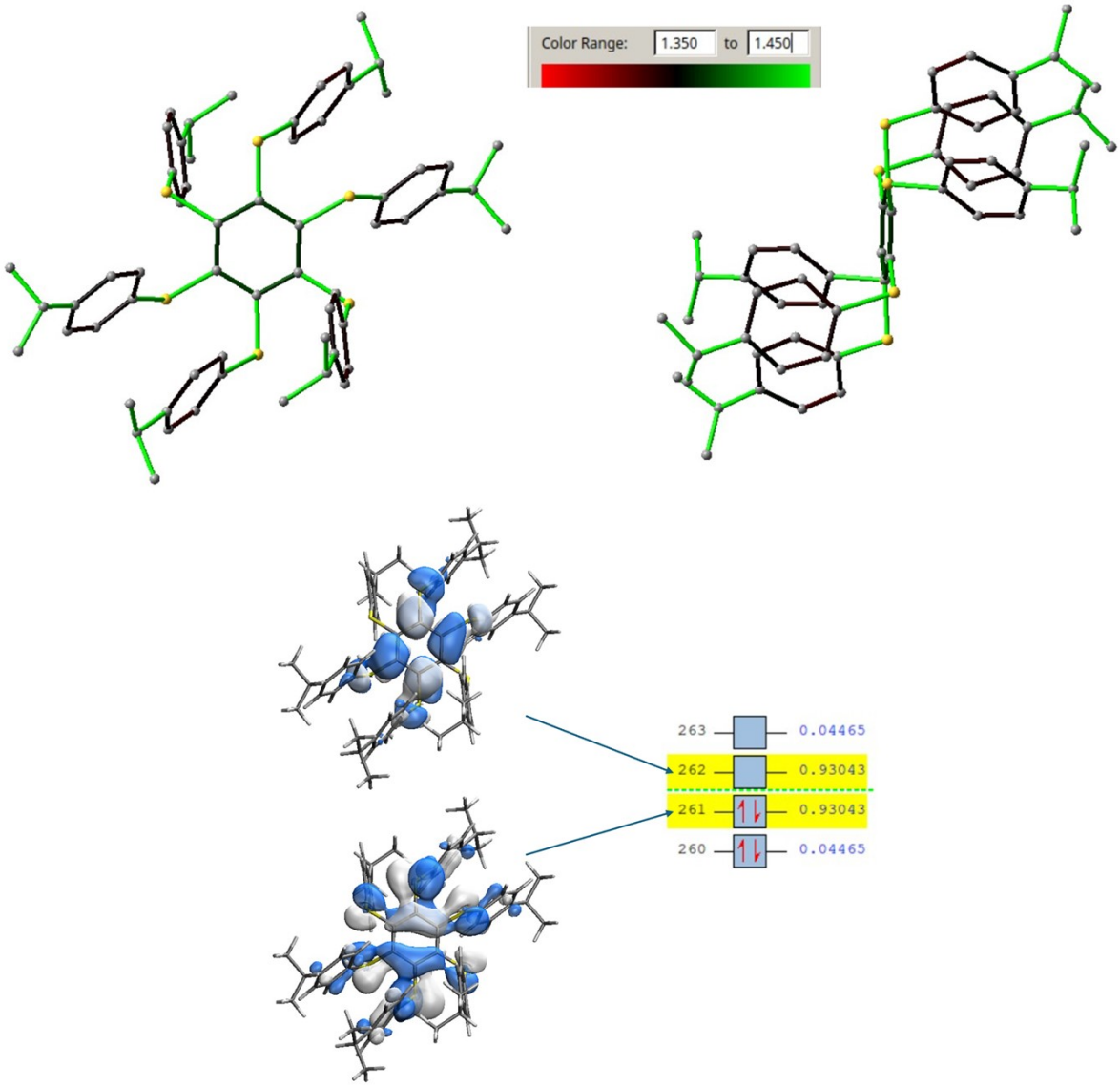

Figure ESI21. A6-iPr, *aaabbb* conformer (Form II): (top) QM/MM optimized ground state geometry (embedded in the crystal) (M06-2X-D3/def2-SVP), hydrogen atoms not shown, color range for bond lengths shown in the inset: aromatic rings appear as dark-grey, markedly double bonds appear in red, longer bonds in green; (bottom) NTO analysis of the lowest triplet excited state showing mixed ππ*/nπ* character (TD-M06-2X-D3/def2-SVP, see Table ESI4).

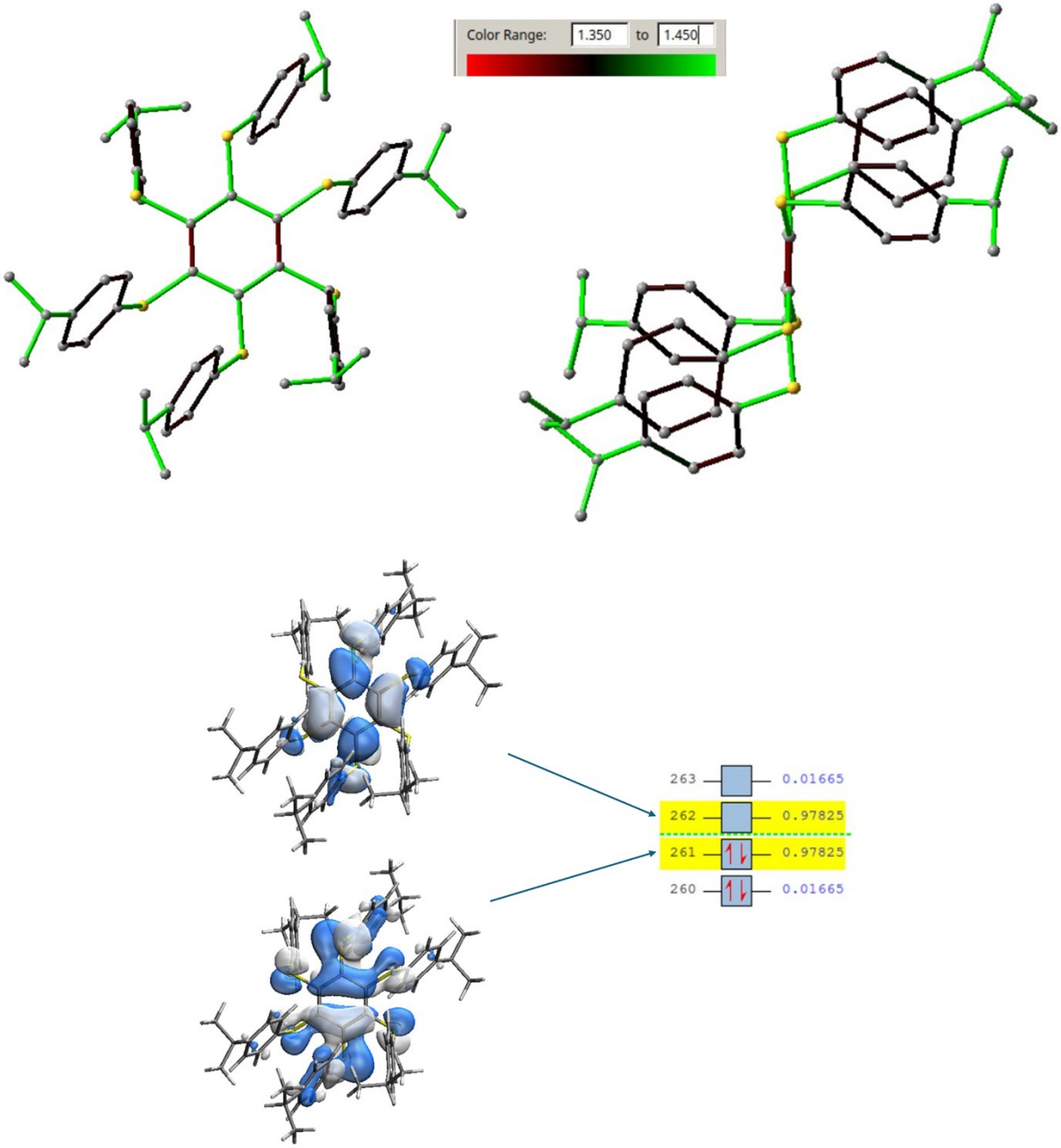

Figure ESI22. A6-iPr, *aaabbb* conformer (Form II): (top) Gas-phase optimized T_1 state geometry (TD-M06-2X-D3/def2-SVP), hydrogen atoms not shown, color range for bond lengths shown in the inset: aromatic rings appear as dark-grey, markedly double bonds appear in red, longer bonds in green. The quinoidal structure of the central ring is clearly seen, due to the localized excitation; (bottom) NTO analysis of the lowest triplet excited state showing side and front view of HONTO and LUNTO (TD-M06-2X-D3/def2-SVP).

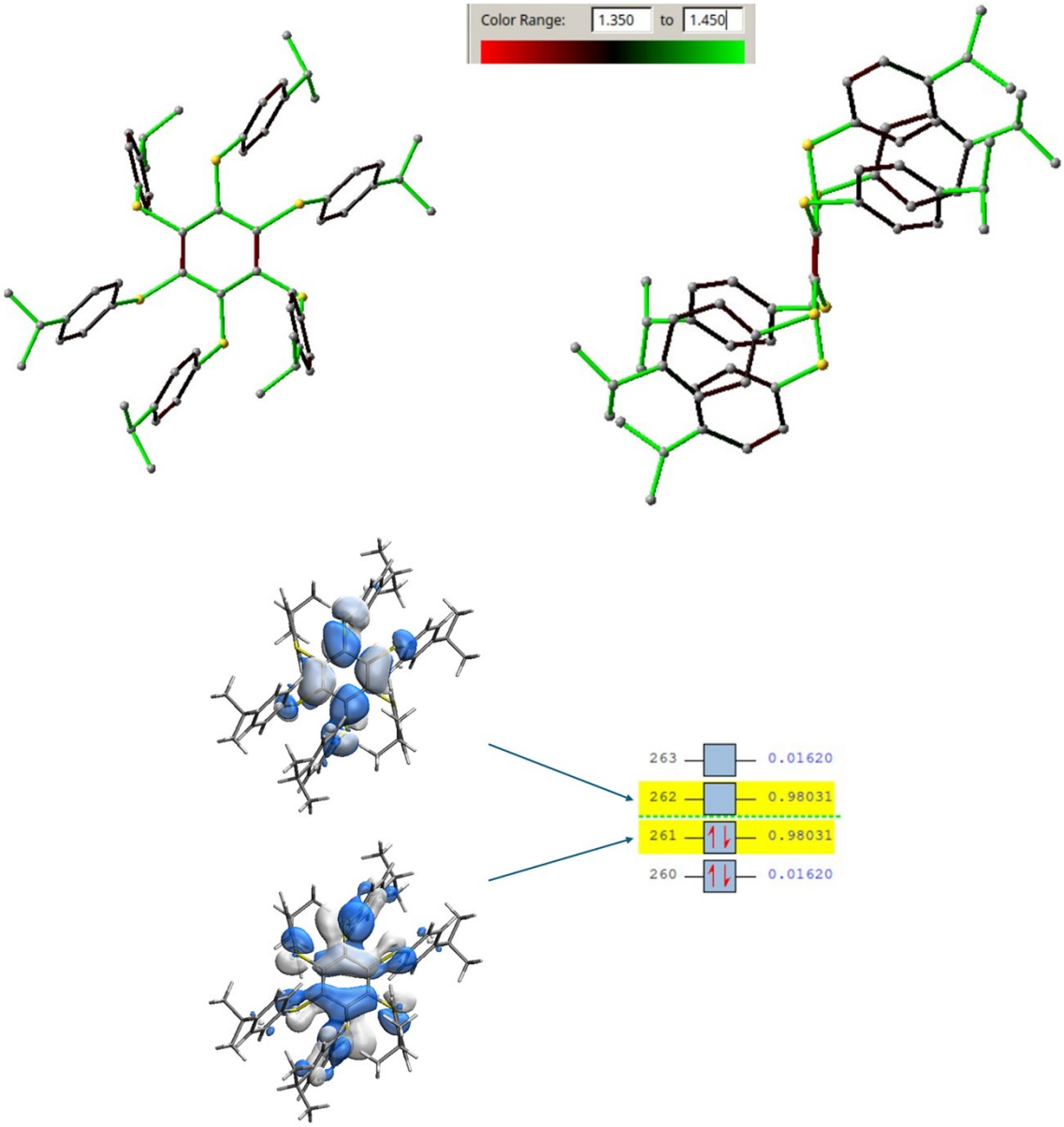

Figure ESI23. A6-iPr, *aaabbb* conformer (Form II): (top) QM/MM optimized T_1 state geometry (embedded in the crystal) (UM06-2X-D3/def2-SVP), hydrogen atoms not shown, color range for bond lengths shown in the inset: aromatic rings appear as dark-grey, markedly double bonds appear in red, longer bonds in green. The quinoidal structure of the central ring is clearly seen, due to the localized excitation; (bottom) NTO analysis of the lowest triplet excited state showing side and front view of HONTO and LUNTO (TD-M06-2X-D3/def2-SVP).

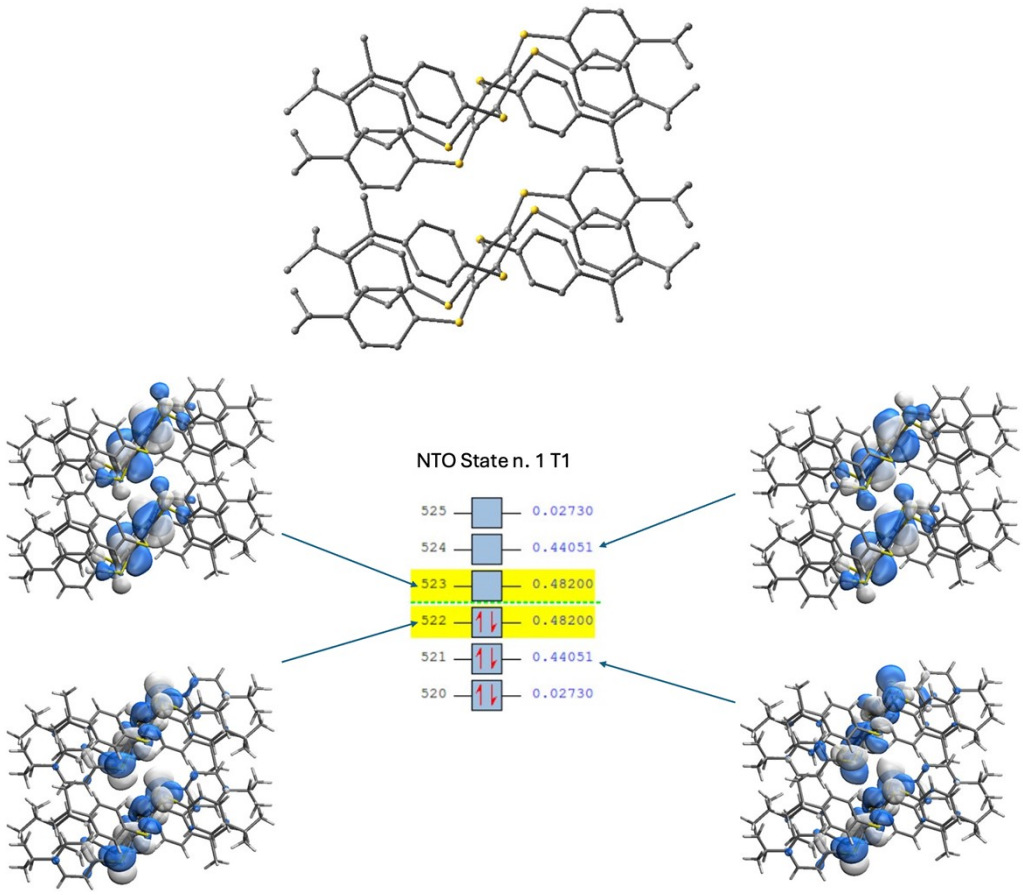

Figure ESI24. A6-iPr, *aaabbb* conformer: (top) dimer structure on which TD-M06-2X-D3/def2-SVP calculations have been carried out. Hydrogen atoms not shown. (bottom) NTO analysis of the lowest triplet excited state (TD-M06-2X-D3/def2-SVP). Numerical results are collected in Table ESI6.

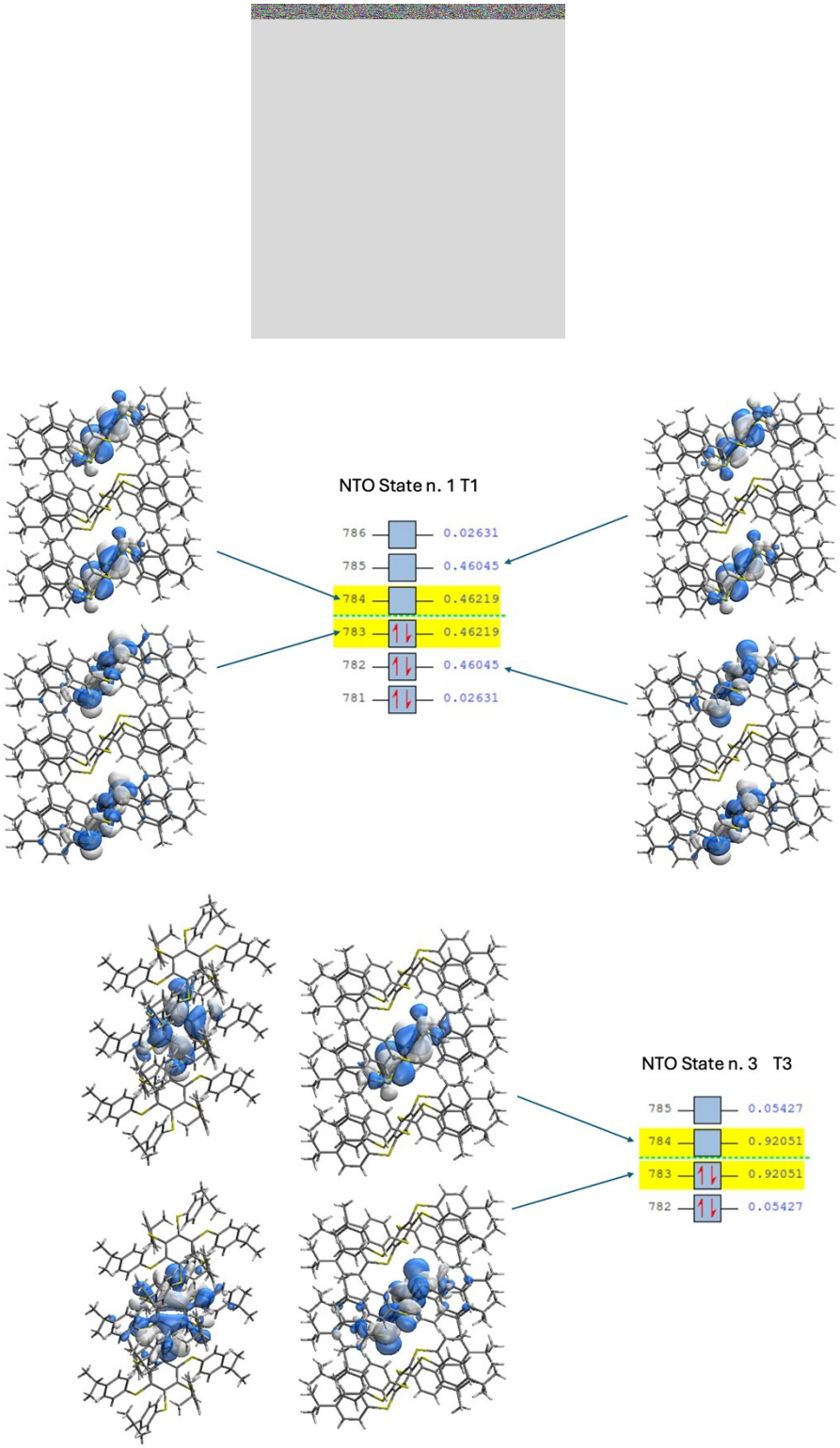

Figure ESI25. A6-iPr, *aaabbb* conformer: (top) trimer structure on which TD-M06-2X-D3/def2-SVP calculations have been carried out. Hydrogen atoms not shown. (bottom) NTO analysis of the triplet excited states T_1 and T_3 (TD-M06-2X-D3/def2-SVP). For the latter, front and side views of the HONTO and LUNTO showing the mixed ππ*/nπ* character. Numerical results are collected in Table ESI6.

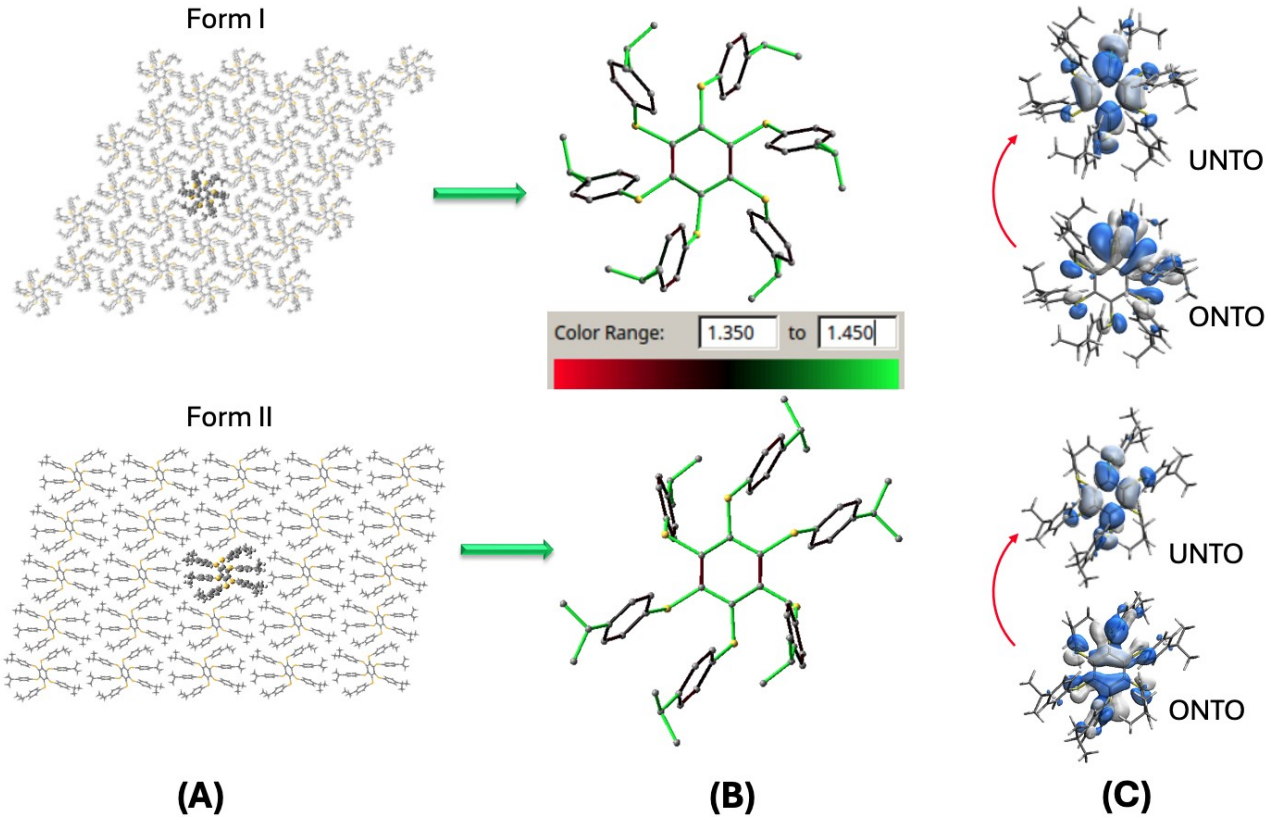

Figure ESI26. Effect of crystal embedding on the nature of the emitting triplet state for Form I and II. (A) supercell used to optimize the T_1 state with QM/MM calculations; (B) optimized triplet state geometry showing the quinoidal structure of the central benzene ring, color range as indicated (distance range in Å); (C) Natural Transition Orbital (NTO) analysis showing the excitation from the occupied NTO (ONTO) to the unoccupied NTO (UNTO) that describe the lowest triplet state.

References

1 G. R. Fulmer, A. J. M. Miller, N. H. Sherden, H. E. Gottlieb, A. Nudelman, B. M. Stoltz, J. E. Bercaw and K. I. Goldberg, *Organometallics*, 2010, **29**, 2176–2179.

2 G. M. Sheldrick, *Acta Crystallogr.*, 2015, **71**, 3–8.

3 G. M. Sheldrick, *Acta Crystallogr.*, 2007, **64**, 112–122.

4 O. V. Dolomanov, L. J. Bourhis, R. J. Gildea, J. A. K. Howard and H. Puschmann, *J. Appl. Cryst.*, 2009, **42**, 339–341.

5 A. Thorn, B. Dittrich and G. M. Sheldrick, *Acta Crystallogr. A*, 2012, **68**, 448–451.

6 C. F. Macrae, I. J. Bruno, J. A. Chisholm, P. R. Edgington, P. McCabe, E. Pidcock, L. Rodriguez-Monge, R. Taylor, J. van de Streek and P. A. Wood, *J. Appl. Crystallogr.*, 2008, **41**, 466–470.

7 M. A. Spackman and D. Jayatilaka, *CrystEngComm*, 2009, **11**, 19–32.

8 S. Suda, A. Tateno, D. Nakane and T. Akitsu, *Int. J. Org. Chem.*, 2023, **13**, 57–85.

9 C. F. Mackenzie, P. R. Spackman, D. Jayatilaka and M. A. Spackman, *IUCrJ*, 2017, **4**, 575–587.

10 P. R. Spackman, M. J. Turner, J. J. McKinnon, S. K. Wolff, D. J. Grimwood, D. Jayatilaka and M. A. Spackman, *J. Appl. Crystallogr.*, 2021, **54**, 1006–1011.

11 J. C. De Mello, H. F. Wittmann and R. H. Friend, *Adv. Mater.*, 1997, **9**, 230–232.

12 A. Fermi, S. d'Agostino, Y. Dai, F. Brunetti, F. Negri, M. Gingras and P. Ceroni, *Chem. Eur. J.*, 2024, **30**, e202401768.

13 S. Grimme, J. Antony, S. Ehrlich and H. Krieg, *J. Chem. Phys.*, 2010, **132**, 154104.

14 M. J. Frisch, G. W. Trucks, H. B. Schlegel, G. E. Scuseria, M. A. Robb, J. R. Cheeseman, G. Scalmani, V. Barone, G. A. Petersson, H. Nakatsuji, X. Li, M. Caricato, A. V. Marenich, J. Bloino, B. G. Janesko, R. Gomperts, B. Mennucci, H. P. Hratchian, J. V. Ortiz, A. F. Izmaylov, J. L. Sonnenberg, D. Williams-Young, F. Ding, F. Lipparini, F. Egidi, J. Goings, B. Peng, A. Petrone, T. Henderson, D. Ranasinghe, V. G. Zakrzewski, J. Gao, N. Rega, G. Zheng, W. Liang, M. Hada, M. Ehara, K. Toyota, R. Fukuda, J. Hasegawa, M. Ishida, T. Nakajima, Y. Honda, O. Kitao, H. Nakai, T. Vreven, K. Throssell, J. A. Montgomery, Jr., J. E. Peralta, F. Ogliaro, M. J. Bearpark, J. J. Heyd, E. N. Brothers, K. N. Kudin, V. N. Staroverov, T. A. Keith, R. Kobayashi, J. Normand, K. Raghavachari, A. P. Rendell, J. C. Burant, S. S. Iyengar, J. Tomasi, M. Cossi, J. M. Millam, M. Klene, C. Adamo, R. Cammi, J. W. Ochterski, R. L. Martin, K. Morokuma, O. Farkas, J. B. Foresman and D. J. Fox, *Gaussian 16, Rev. C. 01*.

15 S. Dapprich, I. Komáromi, K. S. Byun, K. Morokuma and M. J. Frisch, *Journal of Molecular Structure: THEOCHEM*, 1999, **461–462**, 1–21.

16 A. K. Rappe and W. A. Goddard, *J. Phys. Chem.*, 1991, **95**, 3358–3363.

17 S. L. Mayo, B. D. Olafson and W. A. Goddard, *J. Phys. Chem.*, 1990, **94**, 8897–8909.